CELL BIOLOGY

Gatekeeping role of *Nf2*/Merlin in vascular tip EC induction through suppression of VEGFR2 internalization

Jung Hyun Bae[1,2], Myung Jin Yang[1,2], Seung-hwan Jeong[2], JungMo Kim[2], Seon Pyo Hong[2], Jin Woo Kim[3], Yoo Hyung Kim[2]*†, Gou Young Koh[1,2]*

In sprouting angiogenesis, the precise mechanisms underlying how intracellular vascular endothelial growth factor receptor 2 (VEGFR2) signaling is higher in one endothelial cell (EC) compared with its neighbor and acquires the tip EC phenotype under a similar external cue are elusive. Here, we show that Merlin, encoded by the neurofibromatosis type 2 (*NF2*) gene, suppresses VEGFR2 internalization depending on VE-cadherin density and inhibits tip EC induction. Accordingly, endothelial *Nf2* depletion promotes tip EC induction with excessive filopodia by enhancing VEGFR2 internalization in both the growing and matured vessels. Mechanistically, Merlin binds to the VEGFR2–VE-cadherin complex at cell-cell junctions and reduces VEGFR2 internalization–induced downstream signaling during tip EC induction. As a consequence, nonfunctional excessive sprouting occurs during tumor angiogenesis in EC-specific *Nf2*-deleted mice, leading to delayed tumor growth. Together, *Nf2*/Merlin is a crucial molecular gatekeeper for tip EC induction, capillary integrity, and proper tumor angiogenesis by suppressing VEGFR2 internalization.

INTRODUCTION

The key biological process in sprouting angiogenesis is to balance the formation of tip and stalk endothelial cells (ECs), i.e., tip-stalk specification (*1–3*). These two specified EC subtypes are morphologically and functionally distinct, but their formations are closely related. Tip ECs are highly motile with many long and dynamic filopodia and induced by vascular endothelial growth factor A (VEGF-A) (given as VEGF hereafter) signaling (*4, 5*), whereas stalk ECs are highly proliferative with fewer filopodia and regulated mainly by Notch signaling (*1, 2*). These functionally distinct tip and stalk cells coordinate into a branched network of vessels for sprouting angiogenesis (*1–5*). The ECs induced as tip ECs correlatively have a higher delta-like ligand 4 (Dll4) level, which activates Notch signaling in neighboring ECs. High Notch signaling activity inhibits tip EC behaviors while promoting the stalk cell phenotype (*6, 7*). Molecularly, ligand-induced, clathrin-dependent VEGF receptor 2 (VEGFR2) internalization is the initial process for intracellular activation of VEGFR2 signaling (*8–12*), while, morphologically, tip EC induction is a foremost step for sprouting angiogenesis (*13, 14*). However, a persistent puzzle is how one particular EC has higher VEGFR2 signaling activity than its neighbors and is thus fated to become a tip EC during sprouting angiogenesis.

We and others have recently reported that the final effectors of the Hippo pathway, Yes-associated protein (YAP) and its paralog transcriptional coactivator with PDZ-binding motif (TAZ) are essential in the morphogenesis of tip ECs and proliferation of stalk cells (*15–17*). In this biological process, large tumor suppressors 1 and 2 (LATS1/2) act as the direct upstream regulators of YAP/TAZ in the canonical Hippo pathway (*15–17*). Although mammalian sterile 20–like kinase 1 (MST1) acts as an upstream regulator of LATS1/2, we found that MST1 rather promotes nuclear import of FOXO1 (forkhead box O1) in response to hypoxia, leading to endothelial polarity at the tip ECs during sprouting angiogenesis (*18*).

Merlin, encoded by the neurofibromatosis type 2 gene *NF2* (referenced here as *Nf2* for the gene and Merlin for the protein) is ubiquitously expressed in all types of cells and acts as an upstream regulator of the Hippo pathway (*19, 20*). Merlin inactivates the transcriptional activities of YAP/TAZ (*19, 21*) by direct phosphorylation of LATS1/2, which leads to a block of their proteasomal degradations. Beyond Merlin's function in the Hippo pathway (*19*), as a membrane-associated protein, it plays a gatekeeping role in signal transduction from membrane receptors in a cell density–dependent manner (*21–23*). Under low cell density, Merlin is phosphorylated at serine-518 [pMerlin(S518)], which renders the protein inactive (*19, 21*). Inactive Merlin remains in the cytoplasm and allows transduction of membrane receptor signals into cells (*23, 24*). In contrast, at a high cell density, Merlin is dephosphorylated, leading to its activation, which inhibits propagation of the membrane receptor signals (*23, 25*). Active Merlin binds to cadherin-containing complexes and directly suppresses internalization of membrane receptors, such as epidermal growth factor receptor and Notch (*26, 27*). Nevertheless, it has not been investigated whether endothelial Merlin is essential in sprouting angiogenesis and, in detail, which intracellular signaling is regulated by endothelial Merlin.

Here, we unveil that endothelial Merlin is indispensable for tip EC induction by activating intracellular VEGFR2 downstream signaling during sprouting angiogenesis. It forms a complex with VEGFR2 and VE-cadherin and acts as a gatekeeper for VEGFR2 internalization. This entire process seems not to be dependent on the Hippo pathway. Considering different density of VE-cadherin in each EC at angiogenic front (*28*), Merlin in ECs with relatively low VE-cadherin density compared with neighboring ECs allows high VEGF/VEGFR2

[1]Graduate School of Medical Science and Engineering, Korea Advanced Institute of Science and Technology (KAIST), Daejeon 34141, Republic of Korea. [2]Center for Vascular Research, Institute for Basic Science (IBS), Daejeon 34141, Republic of Korea. [3]Department of Biological Sciences, KAIST, Daejeon 34141, Republic of Korea.
*Corresponding author. Email: gykoh@kaist.ac.kr (G.Y.K.); yoohyungk@gmail.com (Y.H.K.)
†Present address: Department of Internal Medicine, Seoul National University Hospital, Seoul 03080, Republic of Korea.

signaling, which leads to tip EC induction. Moreover, Merlin plays a gatekeeping role in maintaining capillary integrity and proper angiogenesis by suppressing unnecessary formation of filopodia and sprouting from the adult normal and tumor vessels.

RESULTS

Endothelial Merlin is a negative regulator in sprouting angiogenesis

To examine the presence of *Nf2* in ECs, we analyzed publicly available data (GSE27238, GSE19284, and GSE86788), which indicated that *Nf2* mRNA expression in retinal ECs was almost equivalent to that of retinal non-ECs in mice at postnatal day 8 (P8) and was similarly expressed in both tip and stalk retinal ECs at P2 (fig. S1, A and B). Moreover, its level was not changed from P6 to P50, while mRNA expressions of tip ECs markers such as EC–specific molecule 1 (*Esm1*), angiopoietin 2 (*Angpt2*), and placental growth factor (*Plgf*) were gradually reduced in the retinal ECs along with postnatal development in mice (fig. S1C). Thus, *Nf2* is equivalently expressed in ECs regardless of developmental stages, as well as in non-ECs.

To investigate the role of endothelial Merlin in sprouting angiogenesis, we generated $Nf2^{i\Delta EC}$ mice by crossing $Nf2^{flox/flox}$ mice (*29*) with *VE-cadherin* Cre-ER^{T2} mice (*30*). With this mutant, we confirmed EC-specific depletion of Merlin by 91.5% but no detectable changes of VE-cadherin and VEGFR2 in lung ECs at 4 days after tamoxifen administration (fig. S1, D to F). Cre-ER^{T2}–positive but flox/flox-negative mice among the littermates were used as wild-type (WT) mice. EC-specific deletion of *Nf2* in $Nf2^{i\Delta EC}$ mice from P2 led to impaired retinal angiogenesis at P6 (Fig. 1A). Compared with WT mice, $Nf2^{i\Delta EC}$ mice exhibited reduced radial length (33.0%) and proliferative 5-ethynyl-2′-deoxyuridine–positive (EdU$^+$) ECs (83.7%) but showed increased vascular branching (3.9-fold), numbers of sprouts (3.2-fold) and filopodia (2.6-fold), vascular density (1.8-fold), and severe vascular leakage at the vascular angiogenic front, whereas filopodial length was comparable between the two animal groups (Fig. 1, B to H). Notably, protein level of ESM1, a marker for tip cell state (*31*), was increased (10.1-fold) in the vascular front in $Nf2^{i\Delta EC}$ mice compared with WT mice at P6 (Fig. 1, E and F). Moreover, EC-specific deletion of *Nf2* in $Nf2^{i\Delta EC}$ mice from P3 led to severely impaired formation of retinal deep vascular plexus, whereas there were 9.9 and 19.9% reductions of radial length and vascular density of retinal superficial vascular plexus at P12 (fig. S2, A to C). To compare EC migration in the presence and depletion of Merlin, we transfected small interfering RNA (siRNA) for control (siCont) or the *NF2* gene (siNF2) into primary cultured human umbilical vein ECs (HUVECs), confirmed knockdown efficiency of the *NF2* gene in siNF2-ECs (HUVECs transfected with siNF2) by immunoblotting for Merlin (85.3% reduction) (fig. S2, D and E), and used the Cell-Insert 2 Well for wounding and migration assay (fig. S2F). Compared with siCont-ECs, siNF2-ECs showed 52.1% less directional migration toward the wounding area (fig. S2, G and H), which is consistent to the findings of the growing retinal vessels in vivo.

To explore whether Merlin regulates Dll4-Notch signaling, we compared protein level of Dll4 in the retinal vascular front of WT and $Nf2^{i\Delta EC}$ mice at P6 and found that the retinal ECs in $Nf2^{i\Delta EC}$ mice had 8.1-fold higher Dll4 compared with those in WT mice (fig. S3, A to C). We also compared mRNA levels of *DLL4*, *HES1*, and *HEY1* between the primary cultured HUVECs transfected with siCont (siCont-ECs) and siNF2 (siNF2-ECs) (fig. S3D). Compared

with siCont-ECs, 1.97-fold increase of *DLL4* but 32.3 and 54.7% reductions of *HES1* and *HEY1* were observed in siNF2-ECs (fig. S3E), implying that Merlin regulates Dll4-Notch signaling by presumably suppressing VEGFR2 signaling. Furthermore, an increased number (2.0-fold) of sprouts were also found in ex vivo cultured aortic rings derived from $Nf2^{i\Delta EC}$ mice compared with those derived from WT mice (fig. S3, F to I). These data indicate that endothelial Merlin is a negative regulator of tip EC induction in sprouting angiogenesis.

Endothelial Merlin negatively regulates tip EC induction by suppressing VEGF/VEGFR2 signaling

Given that VEGF/VEGFR2 signaling is central in sprouting angiogenesis (*1, 2*), we questioned whether *Nf2* deletion in ECs would alter VEGF/VEGFR2 signaling. Gene set enrichment analysis (GSEA) on freshly isolated brain ECs at P9 revealed that in $Nf2^{i\Delta EC}$ compared with WT mice, VEGF target genes and VEGF/VEGFR2 signaling pathway genes were up-regulated [ABE_VEGFA targets, NES (normalized enriched score) = 1.47, $P < 0.01$; WP_VEGFA/VEGFR2 signaling pathway, NES = 1.8, $P < 0.01$; fig. S4B]. Furthermore, in $Nf2^{i\Delta EC}$ mice compared with WT mice, we found up-regulation of *Rspo3*, *Robo1*, *Slit2*, *Esm1*, and *Bmp4*, all genes related to promoting sprouting angiogenesis (fig. S4A).

Accordingly, systemic treatment with DC101 (a VEGFR2-blocking antibody) at P4 and P5 abolished excessive tip EC induction in $Nf2^{i\Delta EC}$ mice (Fig. 2, A to C). The treatment reduced branching points by 71.2% and numbers of filopodia by 71.6% in the retinal vessels compared with control immunoglobulin G (IgG) antibody treatment, whereas these values were 46.8 and 53.4%, respectively, in WT mice (Fig. 2, B and C). To further address the role of endothelial *Nf2* in the response to VEGF stimulation, we compared filopodia formation in siCont-ECs and siNF2-EC after the scratch wounding and VEGF stimulation (Fig. 2D). siCont-ECs and siNF2-ECs showed comparable numbers of phalloidin$^+$ filopodia at the scratch border of the cell membrane. However, VEGF treatment (50 ng/ml) for 6 hours increased the number of phalloidin$^+$ filopodia by 1.9-fold at the leading edge of siCont-ECs (Fig. 2, E and F), notably, by 3.9-fold in siNF2-ECs (Fig. 2, E and F). Moreover, to address the selectivity of Merlin's gatekeeping role in VEGFR2 signaling, we simulated the aortic rings of WT and $Nf2^{i\Delta EC}$ mice with Angpt2, basic fibroblast growth factor (bFGF), lysophosphatidic acid (*LPA*), or VEGF (fig. S5, A and B). Although Angpt2, bFGF, and LPA increased the number of vascular sprouts at different magnitudes in both aortas, no enhancements of vascular sprouting formation were found in the aortas of $Nf2^{i\Delta EC}$ mice compared with those of WT mice (fig. S5, B and C). In comparison, VEGF enhanced vascular sprout formation by 1.7-fold (fig. S5, B and C), implying that endothelial Merlin negatively regulates tip EC induction by selectively suppressing VEGF/VEGFR2 signaling.

Merlin-mediated suppression of tip EC induction is not crucially associated with YAP/TAZ activity

To interrogate whether YAP/TAZ mediates the Merlin-induced suppression of tip EC induction, we generated $Yap/Taz^{i\Delta EC}$ and $Nf2/Yap/Taz^{i\Delta EC}$ mice by crossing double $Yap^{fl/fl}$-$Taz^{fl/fl}$ mice (*32, 33*) and triple $Nf2^{fl/fl}$-$Yap^{fl/fl}$-$Taz^{fl/fl}$ mice with *VE-cadherin*-CreER^{T2} mice (Fig. 3A) and compared vascular phenotypes of growing retinal vessels among them. We used TAZ protein intensity in the retinal vessels as a surrogate marker of YAP/TAZ activity (fig. S6, A and B). TAZ was mainly expressed at the vascular front in WT mice. $Nf2^{i\Delta EC}$
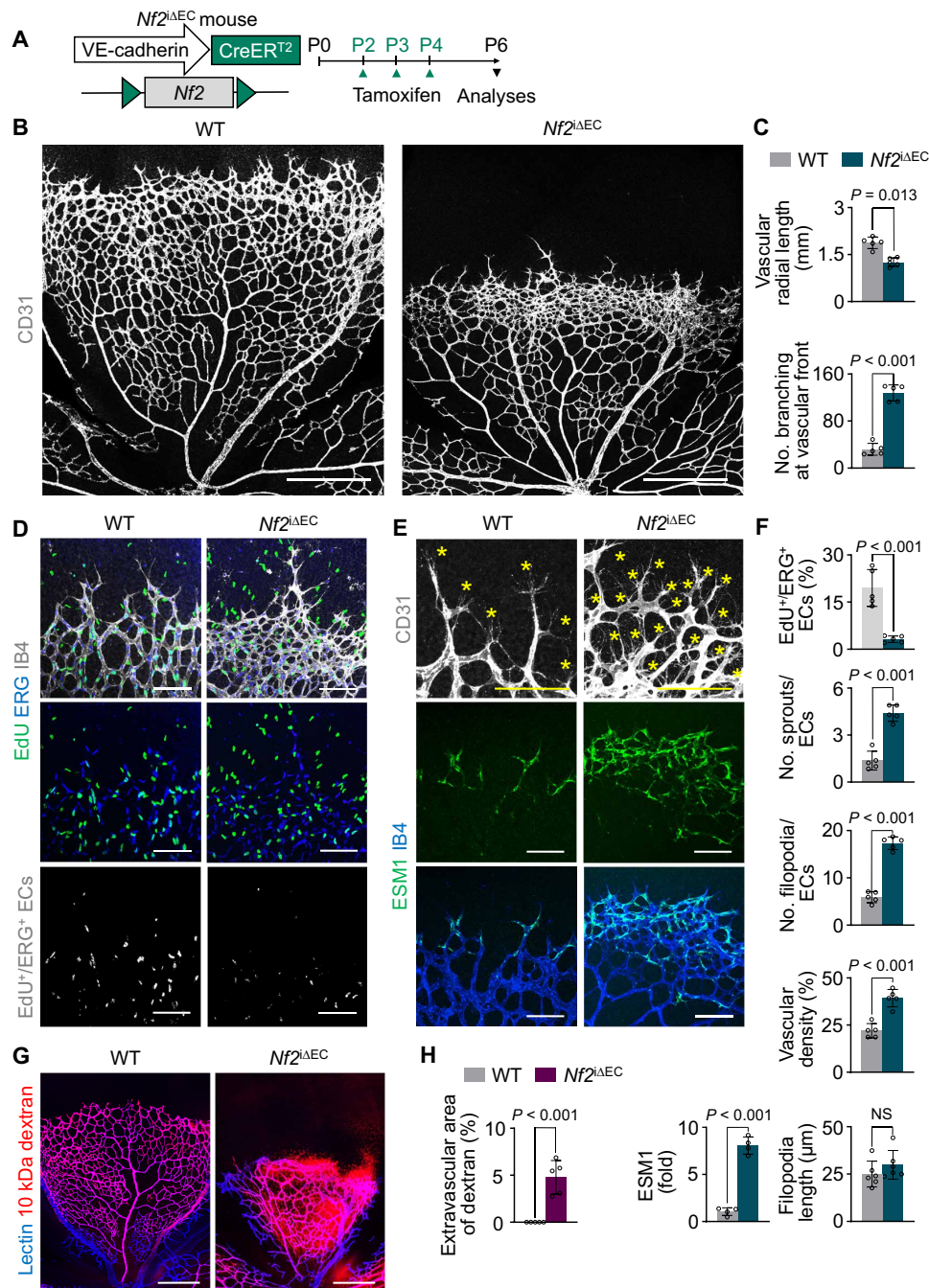
Fig. 1. *Nf2*^iΔEC mice exhibit excessive sprouting and filopodia in the retinal vessels during postnatal development. (**A**) Diagram depicting generation of *Nf2*^iΔEC mouse and experimental schedule for EC-specific deletion of *Nf2* in retinal vessels from P2 and their analyses at P6. (**B** and **C**) Representative images of CD31+ retinal vessels and comparisons of indicated parameters in WT and *Nf2*^iΔEC mice. Scale bars, 500 μm. Each dot indicates a value from one mouse and *n* = 5 mice per group from two independent experiments. Vertical bars indicate means ± SD. *P* values by two-tailed *t* test. (**D** to **F**) Images and comparisons of vascular density, EdU-incorporated proliferating ECs, number and length of filopodia, and ESM1 level at the vascular front of CD31+ retinal vessels in WT and *Nf2*^iΔEC mice. Yellow asterisks indicate tip cells. Scale bars, 100 μm. Each dot indicates a value from one mouse and *n* = 4 to 5 mice per group from three independent experiments. Vertical bars indicate means ± SD. *P* values by two-tailed *t* test. (**G** and **H**) Representative images and comparisons of extravascular dextran leakage in the retinas of WT and *Nf2*^iΔEC mice. Scale bars, 500 μm. Each dot indicates a value from one mouse and *n* = 5 mice per group from two independent experiments. Vertical bars indicate means ± SD. *P* values by two-tailed *t* test.

mice showed elevated TAZ protein intensity (7.8-fold) in both the front and the plexus compared with WT mice, which exhibited no difference in TAZ intensity between the vascular front and plexus. However, both *Yap/Taz*^iΔEC and *Nf2/Yap/Taz*^iΔEC mice showed 88.1

and 94.9% reduced TAZ levels, respectively (fig. S6, A and B). In keeping with what we and others have previously reported (*15–17*), *Yap/Taz*^iΔEC mice had blunt-ended, aneurysm-like structures with few sprouts (95.9% reduction) and limited filopodia formation
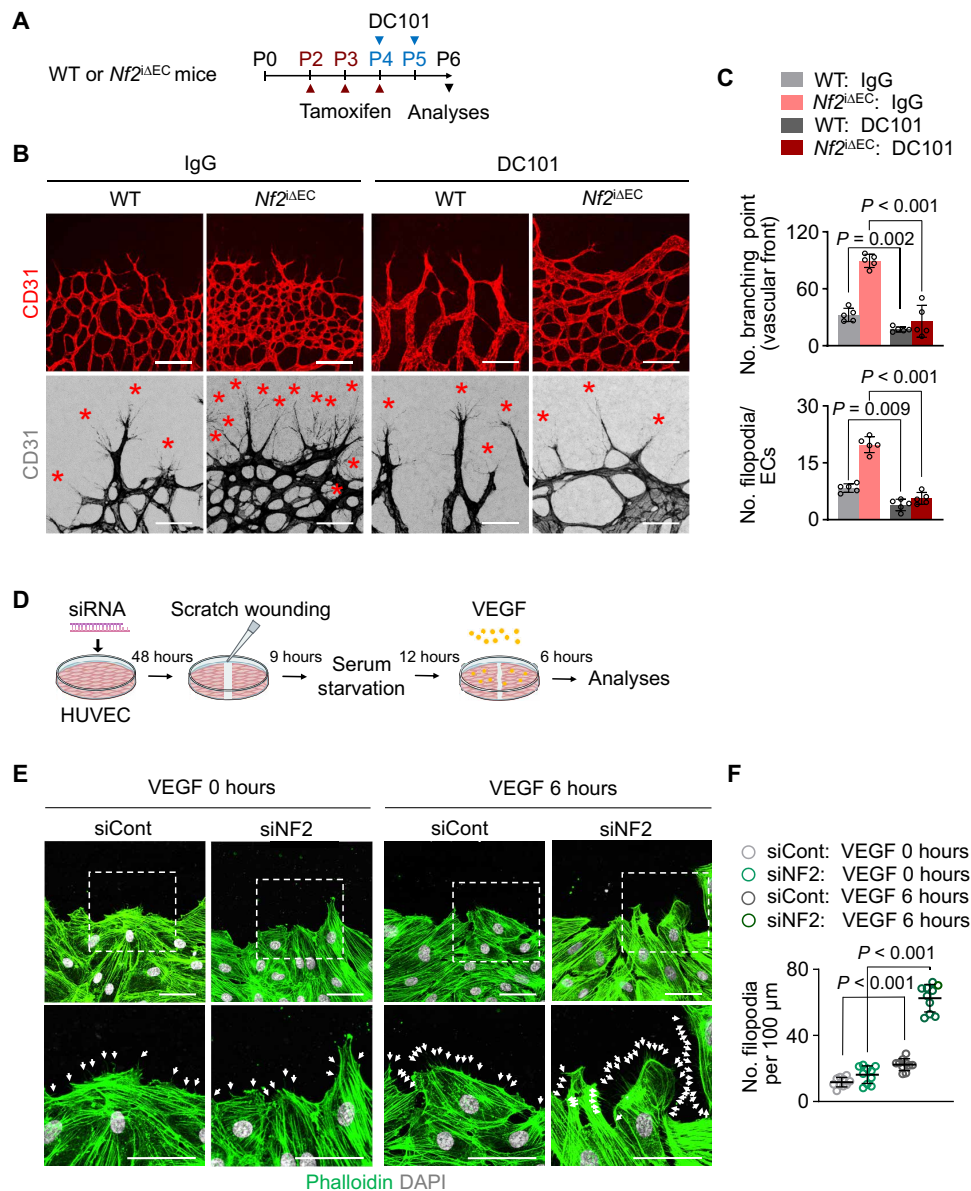
Fig. 2. Endothelial Merlin suppresses tip EC induction by inhibiting VEGF/VEGFR2 signaling. (**A** to **C**) Diagram depicting experimental schedule for tamoxifen administrations, intraperitoneal injections of IgG or DC101 at P4 and P5, and their analyses at P6 in WT and *Nf2*[iΔEC] mice. Images and comparisons of CD31^{+} retinal vessels after DC101 treatment in WT and *Nf2*[iΔEC] mice. Red asterisks indicate tip ECs. Scale bars, 100 μm (top) and 50 μm (bottom). Each dot indicates a value from one mouse and $n = 5$ mice per group from two independent experiments. Vertical bars indicate means ± SD. *P* values by Welch's one-way analysis of variance (ANOVA) test followed by Dunnett's T3 test. NS, not significant. (**D**) Generation of siCont-ECs and siNF2-ECs by transfection of siRNA into HUVECs, scratch wounding with the pipette tip, VEGF (50 ng/ml) treatment for 6 hours, and determination of filopodia formation. (**E** and **F**) Images and comparisons of filopodia formation. Insets (white dashed-line boxes) are magnified in the bottom panels. White arrows indicate phalloidin[+] filopodia. Scale bars, 50 μm. Each dot indicates a value from one cell culture and $n = 10$ per group from three independent experiments. Horizontal bars indicate means ± SD. *P* values by Welch's one-way ANOVA test followed by Dunnett's T3 test. DAPI, 4',6-diamidino-2-phenylindole.

(80% reduction) compared with those of WT mice, whereas *Nf2*[iΔEC] mice exhibited excessive filopodia and hyperplastic vascular growth at the vascular front, as described above (Fig. 3, A to C). Nevertheless, numbers of sprouts and filopodia of *Nf2/Yap/Taz*[iΔEC] mice were higher (2.1- and 1.5-fold) than in WT mice and still similar to those of *Nf2*[iΔEC] mice (Fig. 3, A to C), implying that the Merlin-induced suppression of tip EC induction seems to be not crucially related to the Hippo pathway.

We obtained comparable findings with an ex vivo sprouting assay using the aortic ring derived from the mice (Fig. 3D). Although the aortic ring of *Yap/Taz*[iΔEC] mice formed fewer and shorter sprouts, by 82.3 and 63.9%, respectively, compared with WT mice, the aortic rings of *Nf2/Yap/Taz*[iΔEC] mice formed increased sprout number (1.22-fold) and lengths (1.31-fold) compared with WT animals (Fig. 3, E to F). In addition, both *Nf2*[iΔEC] and *Nf2/Yap/Taz*[iΔEC] mice exhibited comparable number and length of sprouts. Thus, the
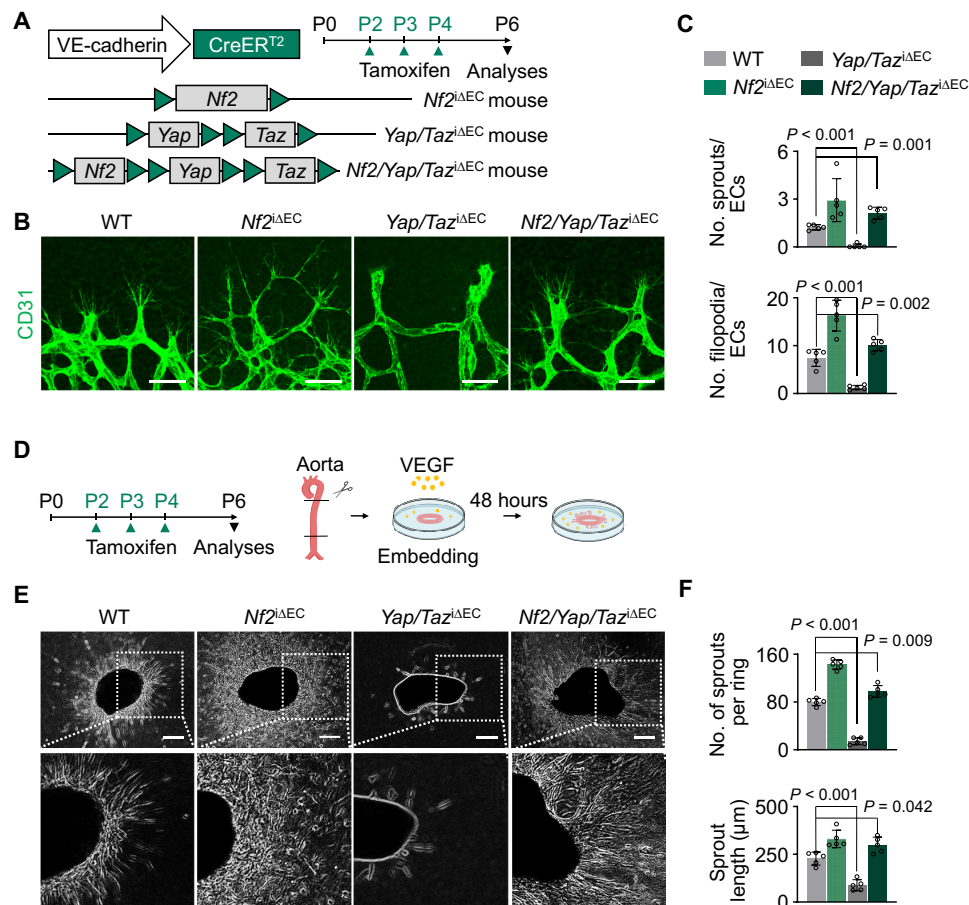
Fig. 3. Endothelial Merlin regulates tip EC induction in an YAP/TAZ-independent pathway during sprouting angiogenesis. (**A** to **C**) Generation of $Nf2^{i\Delta EC}$, $Yap/Taz^{i\Delta EC}$, and $Nf2/Yap/Taz^{i\Delta EC}$ mice and EC-specific deletion of $Nf2$, Yap/Taz, and $Nf2/Yap/Taz$ in retinal vessels from P2 and their analyses at P6. Representative images of CD31$^+$ retinal vessels and comparisons of indicated parameters in WT, $Nf2^{i\Delta EC}$, $Yap/Taz^{i\Delta EC}$, and $Nf2-Yap/Taz^{i\Delta EC}$ mice. Scale bars, 50 μm. Each dot indicates a value from one mouse and $n = 7$ mice per group from five independent experiments. Vertical bars indicate means ± SD. P values by Welch's one-way ANOVA test followed by Dunnett's T3 test. (**D** to **F**) Diagram depicting ex vivo sprouting assay using an aorta ring derived from the mice. Images and comparisons of number and length of sprouts (white) in aortic ring (black in center) of WT, $Nf2^{i\Delta EC}$, $Yap/Taz^{i\Delta EC}$, and $Nf2-Yap/Taz^{i\Delta EC}$ mice. Images in white dashed-line boxes of top panels are magnified in bottom panels. Scale bars, 500 μm. Each dot indicates a value from one mouse and $n = 5$ to 7 mice per group from four independent experiments. Vertical bars indicate means ± SD. P values by Welch's one-way ANOVA test followed by Dunnett's T3 test.

Merlin-induced suppression of tip EC induction again appeared to be unrelated to the Hippo pathways.

Endothelial Merlin negatively governs tip EC induction by reducing VEGFR2 internalization during sprouting angiogenesis

Our GSEA showed up-regulation of genes related to receptor internalization and endocytosis (GO_Receptor internalization, NES = 1.67, $P < 0.01$; KEGG_Endocytosis, NES = 1.366, $P < 0.01$) in $Nf2^{i\Delta EC}$ mice compared with WT mice (fig. S4C). For this reason, we examined spatial regulation of the VEGFR2 trafficking process in growing retinal vessels of WT and $Nf2^{i\Delta EC}$ mice. To visualize distribution of VEGFR2 internalization, we administered Alexa fluorescent dye–labeled VEGF (Fluor-VEGF) intravitreally into the retina at P6 (Fig. 4A). The Fluor-VEGF spots were predominantly localized to the vascular front of retinal vessels at 1 hour but abruptly disappeared at 2 hours after injection in WT mice. In contrast, $Nf2^{i\Delta EC}$ mice compared with WT mice had Fluor-VEGF spots 3.7-fold more localized to the vascular front at 1 hour and reduced at a similar rate but still persistent and 9.8-fold higher at 3 hours after the injection

(Fig. 4, B and C, and fig. S7, A and B). We confirmed the VEGF internalization into the endosome by detection of the colocalization of Fluor-VEGF and early endosomal marker EEA1 (fig. S7, C and D).

Because the major intracellular signaling role of VEGFR2 is activation of extracellular signal–regulated protein kinases 1 and 2 (ERK1/2) and Akt (8, 9), we measured phosphorylated ERK1/2 (pERK1/2) at Thr^{202}/Tyr^{204} and phosphorylated Akt at Ser^{473} in the ECs of growing retinal vessels. pERK1/2 at Thr^{202}/Tyr^{204} and phosphorylated Akt at Ser^{473} was 5.0- and 4.2-fold enhanced in the vascular front of retinal vessels in $Nf2^{i\Delta EC}$ mice compared with WT mice (Fig. 4, D and E, and fig. S7, E and F). Moreover, to delineate whether the VEGFR2 internalization is clathrin dependent, we performed intravitreal injection of dimethyl sulfoxide (DMSO) (5.0% in 0.5 μl) as a control vehicle or Dynasore (200 μM in 0.5 μl), a cell-permeable inhibitor of clathrin-dependent internalization (8, 34), in the neonatal mice.

DMSO did not affect the enhancements of ERK1/2 phosphorylation and numbers of branching points and filopodia in $Nf2^{i\Delta EC}$ mice versus WT mice (Fig. 4, D and E). However, Dynasore largely
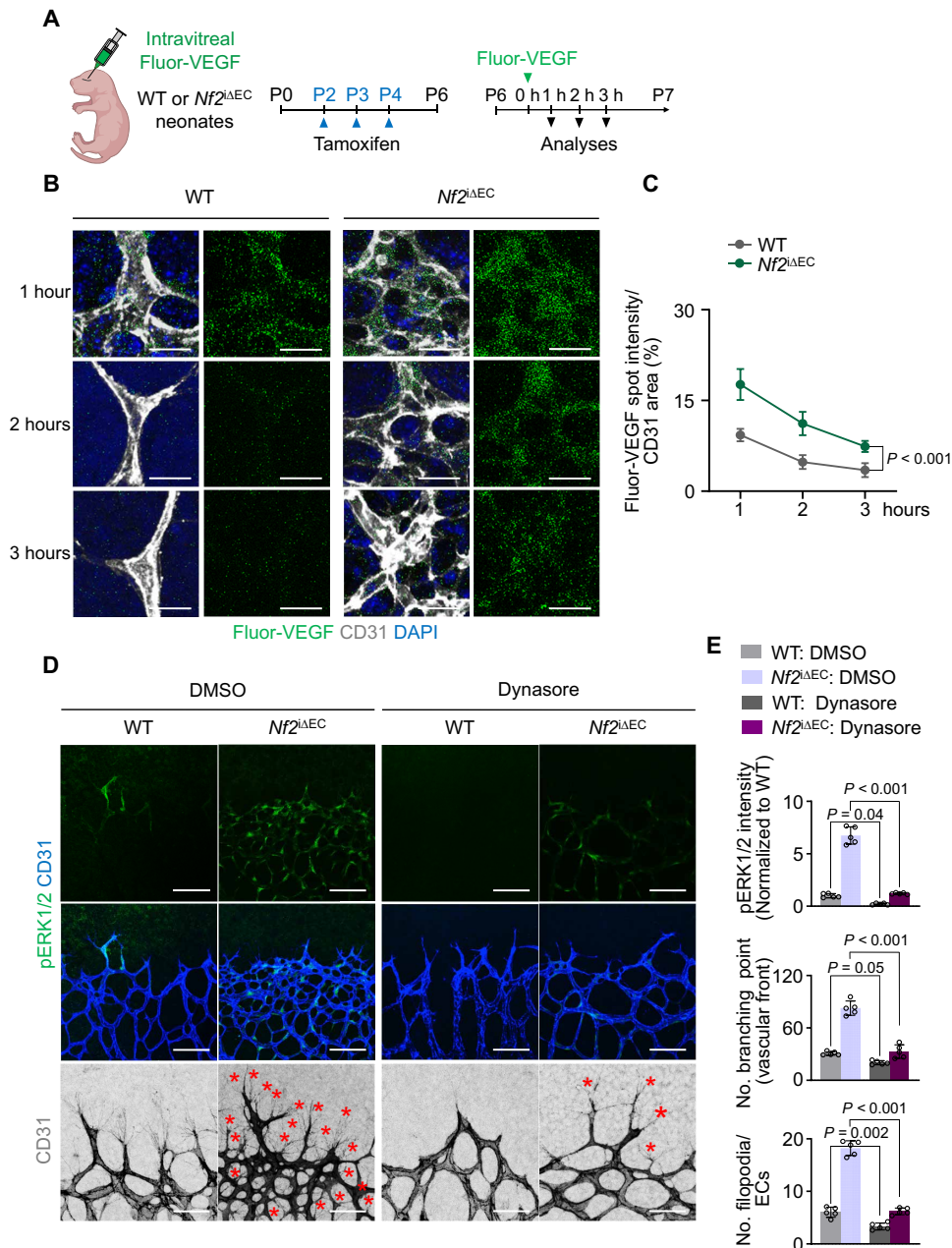
Fig. 4. Endothelial Merlin suppresses tip EC induction by repressing VEGFR2 internalization during sprouting angiogenesis. (**A** to **C**) Diagram depicting experiment for intravitreal injection and follow up of Alexa Fluor 488 dye–labeled VEGF-A (Fluor-VEGF; 0.5 μg in 0.5 μl) in WT and $Nf2^{i\Delta EC}$ neonatal mice. Representative images and comparisons of Fluor-VEGF at the vascular front of retinal vessels in WT and $Nf2^{i\Delta EC}$ mice. Scale bars, 10 μm. Fluor-VEGF spot is presented as percentage per CD31⁺ area. $n = 4$ mice per group from two independent experiments. Dots and bars indicate means ± SD. P values by Welch's one-way ANOVA test followed by Dunnett's T3 test. (**D** and **E**) Images and comparisons of phosphorylated ERK1/2 (pERK1/2) and indicated parameters in the vascular front of CD31⁺ retinal vessels at 24 hours after intravitreal injection of Dynasore (200 μM in 0.5 μl) into WT and $Nf2^{i\Delta EC}$ mice at P5. Red asterisks indicate tip ECs. Scale bars, 100 μm (top and middle) and 50 μm (bottom). pERK1/2 intensity is normalized by those of WT treated with dimethyl sulfoxide (DMSO; 5%, 0.5 μl). Each dot indicates a value from one mouse and $n = 5$ mice per group from three independent experiments. Vertical bars indicate means ± SD. P values by Welch's one-way ANOVA test followed by Dunnett's T3 test.

lessened the enhancements of ERK1/2 phosphorylation and numbers of branching points and filopodia by 81.4, 75.1, and 76.4% in $Nf2^{i\Delta EC}$ mice versus WT mice, respectively (Fig. 4, D and E). To exclude the off-target effect of Dynasore (*34*), we performed the same experiment with intravitreal injection of Pitstop-2 (200 μM in 0.5 μl), a selective and cell membrane–permeable inhibitor of

clathrin-mediated endocytosis by competitively inhibiting clathrin terminal domain (*35*), and obtained comparable results (fig. S8, A to C). Thus, endothelial Merlin negatively regulates tip EC induction by suppressing VEGFR2-ERK1/2 and Akt signaling mainly through inhibiting ligand-induced, clathrin-dependent VEGFR2 internalization.

Endothelial Merlin suppresses VEGFR2 internalization under high cell density through physical interaction with VEGFR2 and VE-cadherin

We examined the localization and density of Merlin in HUVECs under sparse (low cell density, low VE-cadherin density) or dense (high cell density, high VE-cadherin density) culture conditions. Immunofluorescence (IF) staining analysis revealed that Merlin was highly distributed at the cell membrane when ECs were in contact with adjacent ECs under dense culture conditions. In contrast, under sparse culture conditions, Merlin was scarcely distributed at the cell membrane when ECs were not in contact with each other (Fig. 5, A and B). Moreover, Merlin was colocalized with VE-cadherin at the cell membrane (Fig. 5C). Immunoprecipitation with VEGFR2 antibody also indicated that Merlin formed a complex with VEGFR2 and VE-cadherin in HUVECs under dense but less under sparse culture conditions (Fig. 5, D and E). Moreover, the amount of Merlin binding to VEGFR2 was increased as the EC density was increased (fig.S9, A and B). Notably, immunoprecipitation analysis with streptavidin-binding peptide (SBP)–tagged Merlin revealed that Merlin was physically bound to VEGFR2 but not to other representative angiogenic membrane receptor kinases (VEGFR3 and Tie2) (Fig. 5, F and G). To delineate whether VE-cadherin (*CDH5*) is required for the Merlin-VEGFR2 complex formation, we depleted VE-cadherin by transfection of siCDH5 into densely cultured HUVECs (siCDH5-ECs). Immunoprecipitation with VEGFR2 antibody did not pull down a notable amount of Merlin in siCDH5-ECs but pulled down a substantial amount of Merlin in siCont-ECs (Fig. 5, H and I), indicating that VE-cadherin is required for formation of VEGFR2-Merlin complex. Together, these results imply that Merlin exclusively binds to VEGFR2 among the angiogenic receptor tyrosine kinases that form the VE-cadherin–Merlin-VEGFR2 complex at high cell density in HUVECs.

pMerlin(S518) was common in sparsely cultured HUVECs but scarcely detected in densely cultured HUVECs (Fig. 5, J and K). Furthermore, immunoblotting analysis revealed a barely detectable pMerlin(S518) in siCDH5-ECs but detectable in densely cultured siCont-ECs (fig.S9C). To further analyze whether S518 of Merlin is a determinant in the interaction with VEGFR2, HUVECs were transfected with gene constructs encoding Flag-tagged Merlin (Flag-NF2-WT), nonphosphorylatable Merlin (Flag-NF2-S518A), or phosphomimetic Merlin (Flag-NF2-S518D) (fig. S9D). Under dense culture condition, Flag-NF2-WT and Flag-NF2-S518A mutant proteins did bind to VEGFR2 and VE-cadherin, but the Flag-NF2-S518D mutant protein did not (Fig. 5, L to N, and fig.S9E). This finding indicates that interaction between Merlin and VEGFR2 depends on Merlin phosphorylation at S518, under regulation by cell density (fig. S9F).

We further elucidated whether cell density regulates VEGFR2 phosphorylation and internalization and the role of Merlin in these contexts. Phosphorylation of VEGFR2 at Tyr^{1175} was reduced as the EC density was increased (Fig. 6, A and B). To detect only intracellular VEGFR2, we performed an acid wash on HUVECs to remove cell surface–bound VEGF. At 30 min after VEGF treatment, intracellular VEGFR2 was about twofold more internalized in sparsely cultured ECs compared with densely cultured ECs (fig. S10, A and B). Although we found no apparent difference in VEGF-induced VEGFR2 internalization between siCont-ECs and siNF2-ECs under sparse culture conditions, siNF2-ECs showed a 3.7-fold increased VEGF-induced VEGFR2 internalization compared with siCont-ECs

in dense conditions (fig. S10, C and D). Notably, internalized VEGFR2 was 2.4-fold higher and longer after 30 min of VEGF treatment in siNF2-ECs compared with siCont-ECs (Fig. 6, C and D). In contrast, it was less and shorter in Merlin-overexpressed ECs compared with control vector overexpressed ECs (77% less at 30 min of VEGF treatment; Fig. 6, C and D, and fig. S10E). To ensure these changes, we traced intracellular localizations of VEGFR2 in different endosomal compartments by coimmunostaining of VEGFR2 and Rab5 (early endosome), Rab7 (endosomal degradation), or Rab11 (endosomal recycling) in siCont- and siNF2-ECs after 15 min of VEGF treatment (fig. S11, A and B). Localizations of VEGFR2 in early endosome, endosomal degradation, and endosomal recycling compartments were 3.1-, 3.4-, and 3.5-fold higher in siNF2-ECs compared with those in siCont-ECs (fig. S11, A and B).

To further examine whether Merlin phosphorylation on S518 is a critical determinant in VEGFR2 internalization, densely cultured siNF2-ECs were transfected with retrovirus encoding empty gene (Control), Flag-NF2-WT (NF2-WT), Flag-NF2-S518A (S518A), or Flag-NF2-S518D (S518D), stimulated them with VEGF for 15 min and examined VEGFR2 internalization into the early endosomal compartment by covisualization of VEGFR2 and Rab5 (fig. S11C). Compared with Control, NF2-WT and S518A showed 76.1 and 69.3% reductions of VEGFR2 internalization, but S518D showed no difference of VEGFR2 internalization (fig. S11, C and D). Moreover, compared with Control, NF2-WT and S518A showed 62.7 and 68.3% reductions in the VEGF-induced phosphorylation of VEGFR2, VEGFR2 (Y1175), and ERK1/2 (Thr^{202}/Tyr^{204}), but S518D showed no differences of the phosphorylations (Fig. 6, E and F). These findings clarify that Merlin phosphorylation on S518 critically contributes to VEGFR2 internalization and downstream signaling depending on cell density, potentially leading to reduced tip EC induction during sprouting angiogenesis.

Endothelial deletion of Merlin induces excessive VEGF-induced filopodial formation at mature stable vessels

ECs of the vascular plexus have a high density of VE-cadherin and are exposed to low VEGF compared with ECs in the vascular front during sprouting angiogenesis (*4*, *28*, *36*). For this reason, we wondered whether Merlin suppresses tip EC induction in mature ECs through VEGFR2 signaling, as we had found in vitro. Compared with the vascular front, we found less VEGF internalization in the plexus at 3 hours after intravitreal injection of Fluor-VEGF in WT mice (fig. S12, A to D). However, compared with WT mice, VEGF internalization was 7.7-fold increased at 1 hour and rapidly reduced at 2 hours after Fluor-VEGF injection in $Nf2^{i\Delta EC}$ animals (fig. S12, A to D).

To visualize filopodial protrusion in the vascular plexus at the single EC level, we first generated $WT^{i\Delta EC\text{-}TR}$ and $Nf2^{i\Delta EC\text{-}TR}$ mice by crossing $Nf2^{i\Delta EC}$ mice with *Rosa26*-tdTomato reporter mice. We then administered a low dose (0.5 μg) of tamoxifen at P2 for the mosaic induction of tdTomato in the retinal vessels of $WT^{i\Delta EC\text{-}TR}$ and $Nf2^{i\Delta EC\text{-}TR}$ mice (Fig. 7A). Both $WT^{i\Delta EC\text{-}TR}$ and $Nf2^{i\Delta EC\text{-}TR}$ mice exhibited few but a similar number of filopodia in tdTomato$^+$ ECs at the vascular plexus at 6 hours after intravitreal phosphate-buffered saline (PBS) treatment (Fig. 7, B and C). However, at 6 hours after intravitreal VEGF injection, the number of filopodial protrusions increased 3.1-fold in $Nf2^{i\Delta EC\text{-}TR}$ mice compared with $WT^{i\Delta EC\text{-}TR}$ mice (Fig. 7, B and C).

We further examined whether endothelial Merlin still restrains VEGFR2 activation–induced filopodial formation in mature capillary
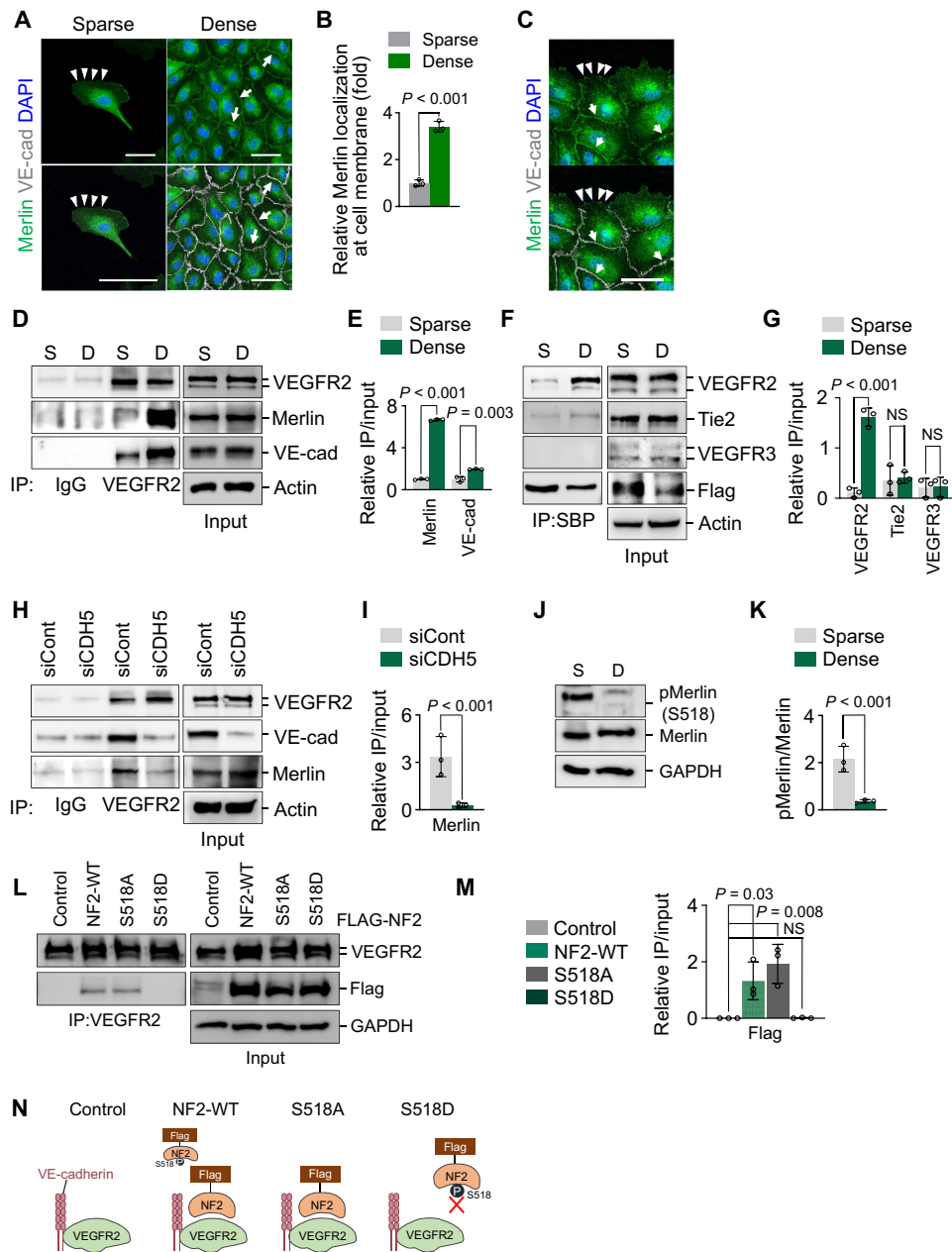
Fig. 5. Dephosphorylated Merlin forms a complex formation with VEGFR2 and VE-cadherin at high cell density. (**A** and **B**) Representative images and comparisons of cell membrane localization of Merlin in sparsely and densely cultured HUVECs. Scale bars, 50 μm. Merlin intensity at cell membrane in sparse HUVECs regards as 1. $n = 3$ per group from two independent experiments. Vertical bars indicate means ± SD. P values by two-tailed t test. (**C**) Images of subcellular localization of Merlin in cell-cell contact (white arrowheads) and no cell contact area (white arrows) in cultured HUVECs. Similar finding was observed in three independent experiments. Scale bar, 50 μm. (**D** to **G**) Immunoblotting and comparison of indicated proteins after immunoprecipitation with SBP-tag, IgG, or anti-VEGFR2 antibody in sparsely (S) and densely (D) cultured HUVECs. $n = 3$ per group from three independent experiments. Vertical bars indicate means ± SD. P values by Welch's one-way ANOVA test followed by Dunnett's T3 test. (**H** and **I**) Immunoblotting and comparison of indicated proteins after immunoprecipitation with IgG or anti-VEGFR2 in densely cultured siCont-ECs and siCDH5-ECs. $n = 3$ per group from three independent experiments. Vertical bars indicate means ± SD. P values by two-tailed t test. (**J** and **K**) Immunoblotting and comparison of phosphorylated Merlin(S518) and Merlin in sparsely and densely cultured HUVECs. $n = 3$ per group from three independent experiments. Vertical bars indicate means ± SD. P values by two-tailed t test. (**L** and **M**) Immunoblotting and quantification of indicated Flag-tagged proteins after immunoprecipitation with anti-VEGFR2 antibody in densely cultured HUVECs transfected with retrovirus encoding empty (Control), Flag-tagged *NF2* (NF2-WT), nonphosphorylatable *NF2* (S518A), or phosphomimetic *NF2* (S518D). $n = 3$ per group from three independent experiments. Vertical bars indicate means ± SD. P values by Welch's one-way ANOVA test followed by Dunnett's T3 test. (**N**) Diagram depicting a proposed model of VEGFR2/Merlin/VE-cadherin interaction.
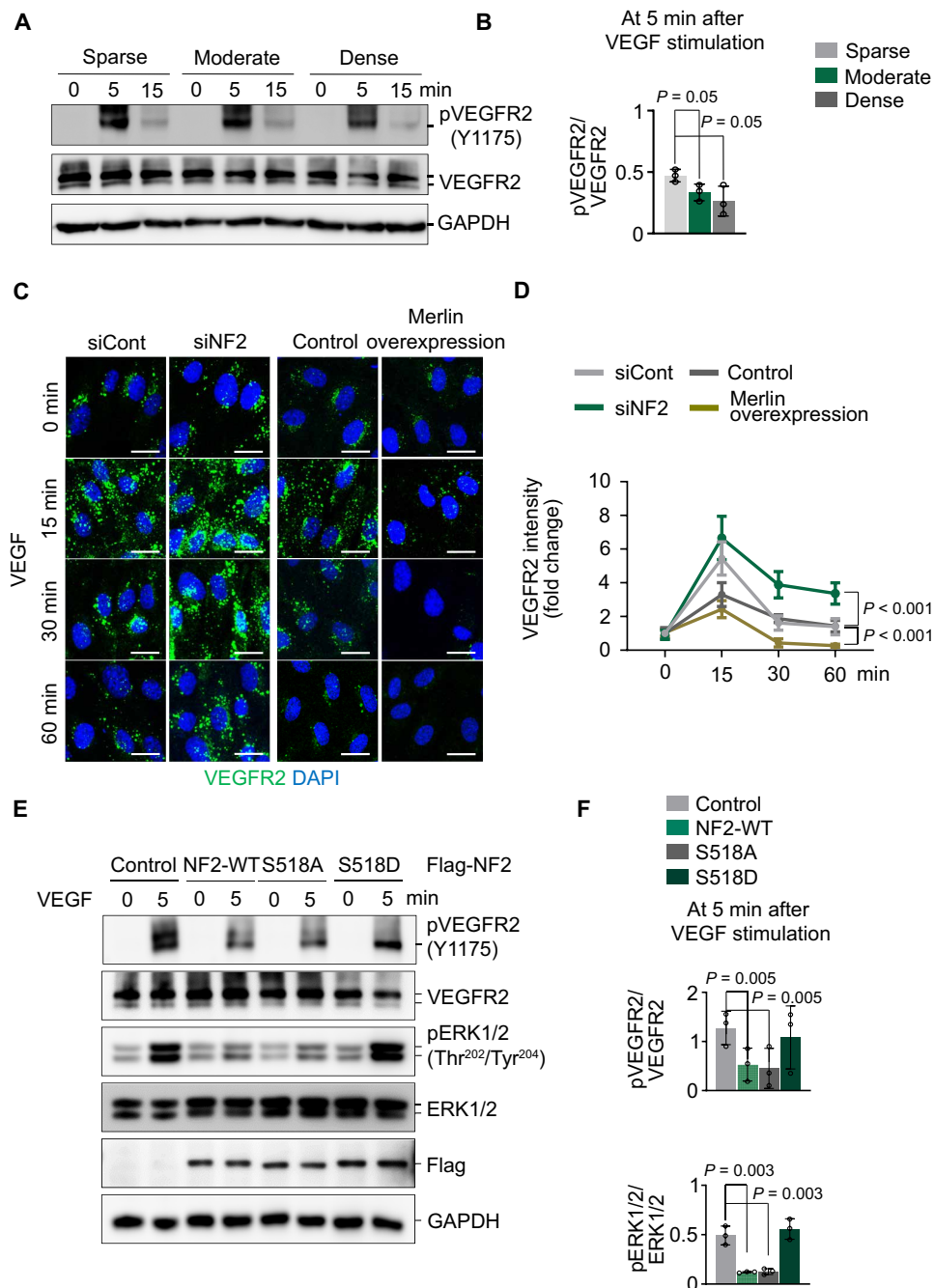
Fig. 6. Merlin limits VEGFR2 internalization and signaling in densely cultured ECs. (**A** and **B**) Immunoblot analyses and comparison of VEGFR2 phosphorylation at Y1175 in sparsely (S), moderately (M), and densely (D) cultured HUVECs for indicated times. $n = 3$ from three independent experiments. Vertical bars indicate means ± SD. P values by Welch's one-way ANOVA test followed by Dunnett's T3 test. (**C** and **D**) Images and comparisons of VEGFR2 internalization rate after VEGF (50 ng/ml) treatment in siCont-HUVECs (siCont), siNF2-ECs (siNF2), or HUVECs transfected with either empty vector (Control) or gene construct encoding NF2 (Merlin overexpression) in densely cultured condition. Scale bars, 20 μm. Dots and bars indicate means ± SD. $n = 6$ per group from three independent experiments. P values by Welch's one-way ANOVA test followed by Dunnett's T3 test. (**E** and **F**) Immunoblot analyses and comparison of phosphorylation of VEGFR2 (Y1175) and ERK1/2 (Thr^{202}/Tyr^{204}) in empty (Control), Flag-NF2-WT, Flag-NF2-S518A, or Flag-NF2-S518D transfected HUVECs at 5 min of VEGF (50 ng/ml) treatment. $n = 3$ from three independent experiments. Vertical bars indicate means ± SD. P values by Welch's one-way ANOVA test followed by Dunnett's T3 test.

ECs of VEGF-enriched organs such as the thyroid gland and small intestinal villi (*37, 38*). In the adult thyroid gland of *Nf2*$^{i\Delta EC}$ mice, vascular density, filopodial number, and extravascular dextran leakage were 1.2-, 3.3-, and 4.8-fold higher than in WT mice (Fig. 7, D to F,

and fig. S13, F and G). Moreover, in the adult small intestinal villi of *Nf2*$^{i\Delta EC}$ mice, filopodial protrusions in the capillary plexus of the jejunum and ileum were respectively 1.8- and 2.8-fold higher than in WT mice (Fig. 7, G and H). In contrast, no apparent differences
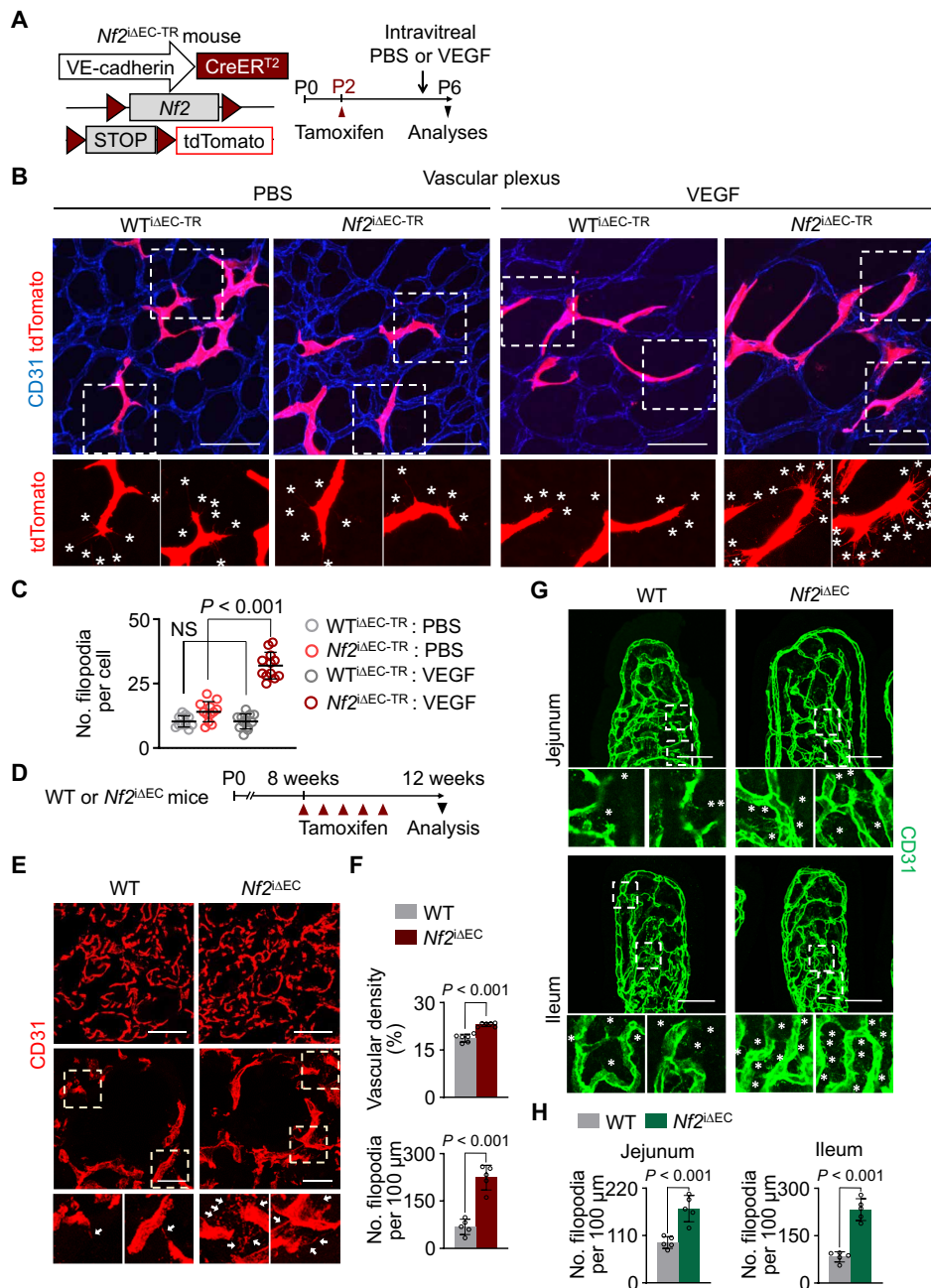
Fig. 7. Endothelial *Nf2* deletion induces aberrant filopodia formation in the matured capillary plexus. (**A**) Diagram for generation of *Nf2*[iΔEC-TR] mice, tamoxifen administration at P2, and the retinas were analyzed at P6. (**B** and **C**) Images and comparison of filopodia in tdTomato[+] retinal ECs of capillary plexus at 6 hours after intravitreal VEGF (0.5 μg in 0.5 μl) treatment in WT[iΔEC-TR] and *Nf2*[iΔEC-TR] mice (*n* = 5, each group). The insets (white dashed-line boxes) are magnified in bottom panels. Scale bars, 50 μm. *n* = 4 mice per group from two independent experiments. Horizontal bars indicate means ± SD. *P* values by Welch's one-way ANOVA test followed by Dunnett's T3 test. (**D**) Diagram depicting experimental schedule for EC-specific deletion of *Nf2* in 8-week-old mice and analyses at 2 weeks later. (**E** and **F**) Images and comparisons of CD31^{+} vascular density and filopodia number per 100 μm of capillary in thyroid gland of WT and *Nf2*[iΔEC] mice. Insets (yellow dashed-line boxes) are magnified in bottom panels. White arrowheads indicate filopodia of tip ECs. Scale bars, 100 μm (top) and 20 μm (bottom). *n* = 5 to 6 mice per group from two independent experiments. Vertical bars indicate means ± SD. *P* values by two-tailed *t* test. (**G** and **H**) Images and comparisons of CD31^{+} filopodia number per 100 μm of capillary plexus in intestinal villi of the indicated part of small intestine of WT and *Nf2*[iΔEC] mice. Insets (white dashed-line boxes) are magnified in bottom panels. White asterisks indicate filopodia of tip ECs. Scale bars, 50 μm. *n* = 5 to 6 mice per group from two independent experiments. Vertical bars indicate means ± SD. *P* values by two-tailed *t* test.

in the vascular density, filopodial number, and extravascular dextran leakage in adult retinas were found between WT and *Nf2*[iΔEC] mice (fig. S13, A to E). Thus, endothelial Merlin acts as a negative rheostat to maintain vascular stability and integrity.

Endothelial Merlin is required to constitute proper tumor angiogenesis

To explore the roles of endothelial Merlin in tumor vessels, we used the subcutaneous Lewis lung carcinoma (LLC) tumor–implanted

model (*39*) in WT and *Nf2*$^{i\Delta EC}$ mice. After 3 weeks of implantation, tumors of *Nf2*$^{i\Delta EC}$ mice were pale and smaller (78.5% less in volume) compared with those of WT mice (Fig. 8, A to C). Notably, compared with tumors of WT mice, those of *Nf2*$^{i\Delta EC}$ mice had an uneven distribution of CD31$^+$ blood vessels with more necrotic areas but had higher (2.2- and 4.3-fold) vascular densities in peri- and intratumoral regions (Fig. 8, D to K). Moreover, lectin-perfused tumor vessels were 88% decreased, and the GLUT1$^+$(glucose transporter 1) hypoxic area
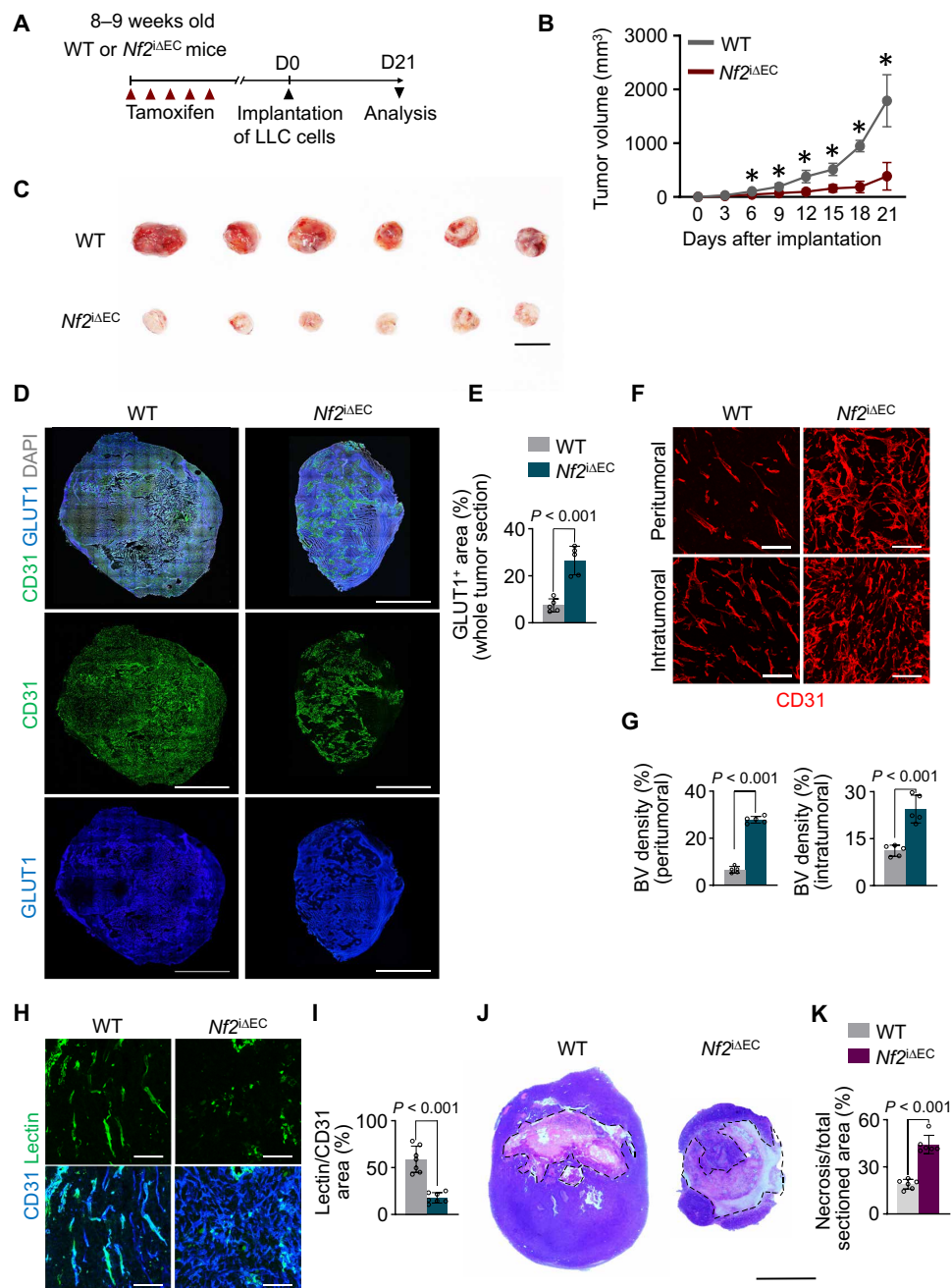

Fig. 8. Endothelial *Nf2* deletion delays tumor growth by generation of nonperfused hypersprouting tumor vasculature. (**A** to **C**) Diagram depicting experimental schedule for EC-specific deletion of *Nf2* in tumor vessels by tamoxifen administration, implantation LLC cells, and their analyses at day 21 after the implantation. Comparison of LLC tumor growth in WT and *Nf2*$^{i\Delta EC}$ mice. Gross findings of LLC tumors harvested at day 21. Scale bar, 10 mm. Dots and bars indicate means ± SD. Plot indicates each individual tumor growth and *n* = 6 mice per group from two independent experiments. *P < 0.05 versus WT by two-tailed *t* test. (**D** to **I**) Representative images and comparisons of GLUT1$^+$ area, blood vessel densities of peri- and intratumoral regions, and lectin perfusion of tumor vessels in the tumors of WT and *Nf2*$^{i\Delta EC}$ mice at day 21 after implantation. Scale bars, 5 mm (D) and 100 μm (F and H). Lectin$^+$ area is presented as a percentage per CD31$^+$ area. Each dot indicates a value from one mouse and *n* = 5 to 6 mice per group from two independent experiments. Vertical bars indicate means ± SD. *P* values by two-tailed *t* test. (**J** and **K**) Hematoxylin and eosin–stained images of tumor sections and comparison of necrotic areas (black dotted line) of tumors harvested on day 21. Necrosis is presented as a percentage per total sectional area. Scale bar, 5 mm. Each dot indicates a value from one mouse and *n* = 6 mice per group from two independent experiments. Vertical bars indicate means ± SD. *P* values by two-tailed *t* test.

was 3.6-fold higher (Fig. 8, D to I). Furthermore, similar phenotypes were observed in $Nf2^{i\Delta EC}$ mice in which Merlin was deleted in tumor vessels after tumor implantation (fig. S14A). After 3 weeks of implantation, $Nf2^{i\Delta EC}$ mice showed 80.6% less tumor volume compared with WT mice (fig. S14, B and C). The peritumoral region of $Nf2^{i\Delta EC}$ mice had a vessel density comparable to that of WT mice, but vessel density in the intratumoral region of $Nf2^{i\Delta EC}$ mice was 2.8-fold compared with WT animals (fig. S14, D to G). In addition, tumor vascular perfusion of $Nf2^{i\Delta EC}$ mice was impeded by 30%, but tumors had 2.7- and 2.3-fold more hypoxic area and necrotic area, respectively, compared with WT mice (fig. S14, F to I). Thus, endothelial Merlin is required to constitute proper and patent tumor vessels.

Specification into endothelial tip and stalk cells is strictly dependent on Merlin in tumor angiogenesis

To gain further insight into the roles of endothelial Merlin in tumor vessels, we performed single-cell RNA sequencing (scRNA-seq) on the tumor ECs of implanted LLC tumors of WT and $Nf2^{i\Delta EC}$ mice (Fig. 9A). Through unsupervised clustering, we identified four distinct subpopulations: tip-like, stalk-like, transitional, and proliferative ECs (Fig. 9B and fig. S15) (40, 41). Notably, compared to tumor ECs of WT mice, those of $Nf2^{i\Delta EC}$ mice exhibited an enriched tip-like EC population but a reduced stalk-like EC population (Fig. 9C). Through Gene Ontology (GO) term analysis with Enrichr (42), we found that VEGFA-VEGFR2 signaling, ERK1/2 cascade, endocytosis regulation, and the VEGFR signaling pathway of WikiPathways and GO biological processes were up-regulated in tumor ECs of $Nf2^{i\Delta EC}$ mice compared with those of WT mice (Fig. 9D). Consistently, ECs of $Nf2^{i\Delta EC}$ mice showed up-regulated expression of genes related to tip ECs, hypoxia, endocytosis, and ERK signaling (Fig. 9E). Accordingly, compared with WT mice, $Nf2^{i\Delta EC}$ mice showed a 9.1-fold higher population of placental growth factor$^+$ (PlGF$^+$; a representative marker for tip-like ECs) in tumor vessels but 78.3% less atypical chemokine receptor 1$^+$ (ACKR1$^+$; a representative marker for stalk-like ECs) (Fig. 9, F and G). Thus, our scRNA-seq analysis confirmed that $Nf2$ governs specification of tip or stalk cells and that lack of Merlin in tumor ECs up-regulates genes related to VEGFR2 endocytosis, hypoxia, and ERK signaling.

DISCUSSION

In this study, we show that Merlin is mainly localized at the cell membrane in vascular ECs, interacts with VEGFR2 and VE-cadherin, and plays a negative role in VEGFR2 intracellular downstream signaling by suppressing VEGFR2 internalization. As a consequence, endothelial Merlin is a gatekeeping regulator for tip EC induction in retinal sprouting angiogenesis during postnatal development, for formations of filopodia and sprouts in matured and established capillary ECs of adults, and for tip cell formation and proper tumor vessel construction in tumor vessels (Fig. 10).

Our analyses of in vivo retinal angiogenesis and the ex vivo aortic ring assay using $Nf2^{i\Delta EC}$ mice clearly show that endothelial Merlin is a negative regulator of tip EC induction in sprouting angiogenesis. Given that VEGF/VEGFR2 signaling is central in sprouting angiogenesis (1, 2), we questioned whether $Nf2$ deletion in ECs alters VEGF/VEGFR2 signaling. The GSEA revealed that $Nf2$ suppresses the genes related to VEGF/VEGFR2 signaling and sprouting angiogenesis. In line with this finding, VEGFR2 blockade abolished

excessive tip EC induction in $Nf2^{i\Delta EC}$ mice, whereas VEGFR2 stimulation potentiated filopodia formation at the wounding site of cultured $Nf2$-deleted ECs. These results indicate that endothelial Merlin negatively regulates tip EC induction by suppressing VEGF/VEGFR2 signaling. In addition, our findings suggest that Merlin Dll4-Notch regulates signaling by presumably suppressing VEGFR2 signaling for proper tip cell/stalk cell formation in sprouting angiogenesis. Because Dll4-Notch signaling is a critical regulator for tip cell induction (1, 2, 6, 7), a more detailed mechanistic study regarding the roles of Merlin on Dll4-Notch signaling in the tip cell induction is warranted in the future. On the other hand, although Merlin acts as a suppressor of YAP/TAZ transcriptional coactivators through canonical signaling (19, 20), our findings using combined and EC-specific gene deletions in mice indicate that Merlin-mediated suppression of tip EC induction is not critically mediated through the Hippo pathway.

Ligand-induced, clathrin-dependent VEGFR2 internalization is the initial cellular process for downstream activation of VEGFR2 signaling (8–12), which leads to sprouting angiogenesis, including tip EC induction (13, 14). Our in vivo VEGFR2 internalization analysis using growing retinal vessels convincingly demonstrated that endothelial $Nf2$ deletion prolongs VEGF internalization into the ECs during sprouting angiogenesis. Moreover, major intracellular signaling of VEGFR2, pERK1/2 (Thr^{202}/Tyr^{204}), and pAkt (Ser473) was enhanced, and blockade of clathrin-dependent internalization largely abolished pERK1/2 (Thr^{202}/Tyr^{204}) and reduced the number and length of filopodia in the ECs of growing retinal vessels in $Nf2^{i\Delta EC}$ mice. On the basis of these findings, we conclude that endothelial Merlin negatively regulates tip EC induction by suppressing VEGFR2-ERK1/2 and Akt signaling mainly through inhibiting ligand-induced, clathrin-dependent VEGFR2 internalization.

We found that Merlin is highly localized at the cell membrane when ECs are in contact with adjacent ECs under dense culture conditions but scarcely localized at the cell membrane when ECs are in contact with adjacent ECs under sparse culture conditions. Notably, Merlin engages in a physical interaction with VEGFR2 and VE-cadherin in dense culture, which has a low pMerlin(S518), but Merlin does not engage in this interaction in sparse culture, with a high pMerlin(S518) in cultured ECs. Thus, interaction between Merlin and VEGFR2 depends on pMerlin(S518), which is regulated by cell density (43). Considering different densities of VE-cadherin in each EC at the angiogenic front (28), inactivated Merlin in ECs with relatively low VE-cadherin density contributes to tip EC induction through relatively high VEGF signals compared with neighboring ECs with high VE-cadherin density (Fig. 9). However, given that endothelial tip and stalk cells, either in physiological or pathological contexts, are in close contact with neighboring cells in vivo, both gatekeeping role of Merlin in VEGFR2 signaling and the adherens junctions may critically contribute to VE-cadherin dynamics and stability for proper sprouting angiogenesis and maintaining EC integrity.

Our data reveal that VEGFR2 internalization is differently regulated in sparse and dense culture conditions. Sparsely cultured HUVECs had an about twofold higher VEGFR2 internalization than densely cultured ECs. In contrast, Merlin-depleted ECs showed increased VEGFR2 internalization, whereas Merlin-overexpressed ECs showed reduced VEGFR2 internalization under dense culture conditions. In line, Lampugnani et al. (44) reported that VE-cadherin restricts VEGFR2 internalization and intracellular signaling by making complex with β-catenin and DEP-1 (density-enhanced phosphatase-1)
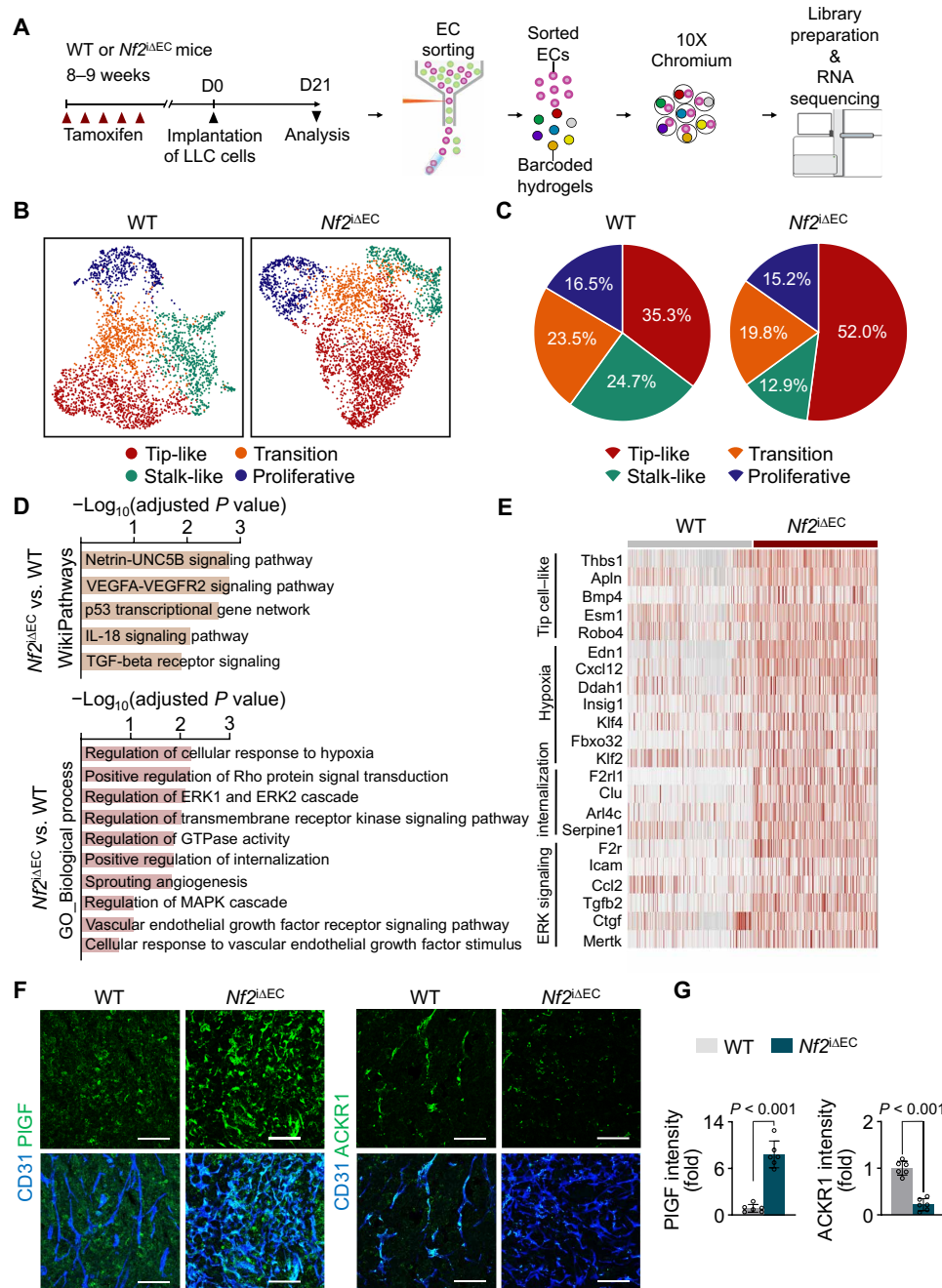
Fig. 9. Endothelial *Nf2* deletion produces more tip-like ECs, while it reduces stalk-like ECs in tumor vessels. (**A**) Diagram depicting tamoxifen administration and implantation of LLC cells into WT and *Nf2*^iΔEC mice, harvesting tumors and sorting of tumor ECs at day 21, and performing single-cell RNA analysis. (**B**) Uniform manifold approximation and projection plots visualizing four clusters of tumor ECs by unsupervised clustering in WT and *Nf2*^iΔEC tumor EC datasets. (**C**) Pie chart depicting compositions of tumor EC subpopulations in WT and *Nf2*^iΔEC datasets. (**D**) Significantly enriched pathways and GO terms in *Nf2*^iΔEC over WT tumor ECs. Bars indicate significance defined as −log$_{10}$adjusted *P* values. (**E**) Heatmap visualizing scaled expression of genes related to tip cells, hypoxia, internalization, and ERK signaling in WT and *Nf2*^iΔEC tumor ECs. (**F** and **G**) Representative images and comparisons of PlGF^+/CD31^+ tip-like tumor ECs and ACKR1^+/CD31^+ stalk-like tumor ECs between WT and *Nf2*^iΔEC mice. Scale bars, 100 μm. Each dot indicates a value from one mouse and *n* = 6 mice per group from two independent experiments. Vertical bars indicate means ± SD. *P* values by two-tailed *t* test.

at EC-EC contact in dense culture conditions, while this restriction is released in sparse culture conditions. These findings indicate that Merlin, together with membrane-associated β-catenin and phosphatase DEP-1, is a critical, negative rheostat in VEGFR2 internalization and that its main downstream signaling activation

depends on cell density, which leads to proper formation of tip ECs during sprouting angiogenesis.

We also questioned whether endothelial Merlin acts as a negative rheostat in matured vessels of VEGF-enriched organs, including thyroid gland and intestinal villi (*37*, *38*). *Nf2*^iΔEC mice
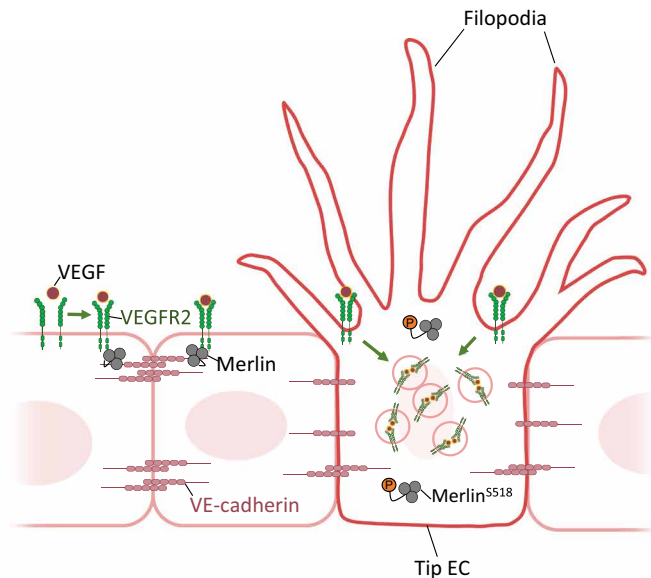
Fig. 10. Endothelial Merlin plays a gatekeeping role in tip EC induction mediated through blocking VEGFR2 internalization at high VE-cadherin density. Schematic diagram depicting roles of Merlin in different density of VE-cadherin in each EC. Active Merlin forms complex with VEGFR2 and VE-cadherin at relatively high VE-cadherin density, while inactive Merlin (S518) allows high VEGFR2 internalization in ECs with low VE-cadherin density, which leads to tip EC induction.

showed highly increased filopodial protrusions in the capillaries of thyroid gland and small intestinal villi, indicating that endothelial Merlin acts as a negative switch on filopodia formation in mature ECs. This continuous action of endothelial Merlin in VEGF-enriched organs could contribute to maintaining stable blood capillary integrity.

As one of most evident phenotypic hallmarks of cancer, tumor angiogenesis is a critical pathophysiological process for meeting unregulated tumor growth (45). Tumor angiogenesis has been an attractive target for antitumor therapy, but antiangiogenic therapies have proved less effective than anticipated, mostly because they worsen severe hypoxia, the underlying cause of the proangiogenic drive in cancer (45–47). Merlin in the neuronal cells plays a gatekeeping role in physiologic angiogenesis by promoting secretions of antiangiogenic factors such as SEMA3F (semaphorin 3F) (48). Thus, similar to the case of mutation of *NF2* gene in NF (19), the loss of Merlin contributes to promote tumor angiogenesis in the neuronal tissues (48). Nevertheless, because tumor angiogenesis is largely dependent on activation of VEGF-VEGFR2 signaling in the ECs (49, 50), we explored the roles of endothelial Merlin in this process using an implanted LLC tumor model in $Nf2^{i\Delta EC}$ mice. As expected, the relative vascular density and population of tip-like cells and the genes related to VEGFR2 endocytosis and signaling and ERK signaling were higher in the tumor vessels of $Nf2^{i\Delta EC}$ compared with WT mice. However, the tumor growth was paradoxically delayed, mainly because of a lack of blood perfusion into the highly vascularized tumor in the $Nf2^{i\Delta EC}$ mice. Supporting these findings, tumors grown in $Nf2^{i\Delta EC}$ mice were extremely hypoxic and had more necrotic areas. These paradoxical findings are in line with the finding that blockade of DLL4 delays tumor growth by promoting nonproductive angiogenesis (51, 52). Thus, tumor EC Merlin is required for development of sufficient tumor vessels for blood supply to the growing tumor, and it presents an attractive target for disrupting tumor vasculature and delaying tumor growth.

MATERIALS AND METHODS
Mice and treatment
Specific pathogen–free (SPF) C57BL/6J and R26-tdTomato mice were purchased from the Jackson Laboratory. *VE-cadherin*-CreER^T2 (30), *Nf2^{fl/fl}* (29), *Yap^{fl/fl}* (33), and *Taz^{fl/fl}* (32) mice were transferred, established, and bred in our SPF animal facilities at Korea Advanced Institute of Science and Technology (KAIST) and fed with free access to a standard diet (PMI LabDiet) and water. To induce Cre activity in the CreER^T2 mice, tamoxifen (Sigma-Aldrich, T5648) was given with the following dosages and schedules: For neonatal mice, 100 μg of tamoxifen dissolved in corn oil (Sigma-Aldrich, C8267) was injected into the stomach daily from P2 to P4 or P3 to P5. A total of 0.5 μg of tamoxifen was injected into the stomach at P2 for mosaic deletion. For adult mice aged 7 to 8 weeks, 2 mg of tamoxifen was injected intraperitoneally for five consecutive days. For in vivo inhibition of VEGF/VEGFR2 signaling, DC101 (40 mg/kg) (BioXcel, BE0060) was injected subcutaneously into the mice at P4 and P5 and the retinas were harvested at P6. Recombinant mouse VEGF (0.5 μg in 0.5 μl) (R&D Systems, 493-MV), Dynasore (200 μM in 0.5 μl; Sigma-Aldrich), or Pitstop-2 (200 μM in 0.5 μl, Abcam) was injected into vitreous cavity using Nanoliter 2000 micro-injector (World Precision Instruments) fitted with a glass capillary pipette. All mice were anesthetized by intraperitoneal injection of a combination of anesthetics [ketamine (80 mg/kg) and xylazine (12 mg/kg)] before all the procedures and being sacrificed. Animal care and experimental procedures were performed under the approval from the Institute Animal Care and Use Committee (no. KA2018-79) of KAIST.

Histological analyses
Eyeballs of neonatal mice were enucleated and fixed in 4% paraformaldehyde (PFA) for 20 min at room temperature (RT). After dissecting the retinas from eyeballs, they were additionally fixed in 1% PFA for 1 hour at RT followed by several washes. Embedding of aortic rings in collagen gel was fixed in 4% PFA for 30 min at RT followed by several washes. HUVECs were fixed 2% PFA for 10 min at RT and permeabilized with PBST (0.1% Triton X-100 in PBS). Implanted LLC tumors were harvested and fixed in 4% PFA at 4°C for 6 hours, dehydrated in 30% sucrose solution for 48 hours, and embedded in tissue-freezing medium (Leica). Frozen blocks were cut into 30-μm sections. Thyroid glands were harvested and fixed in 4% PFA at 4°C for 1 hour, dehydrated in 30% sucrose solution for 20 hours, and embedded in tissue freezing medium (Leica). Frozen blocks were cut into 20-μm sections. Small intestine was harvested and cut longitudinally to expose the lumen. After several washes with PBS, intestines were pinned on silicon plates. Samples were then postfixed at 4% PFA at 4°C for 2 hours. Samples were washed with PBS for 2 hours and with 20% sucrose and 10% glycerol in PBS overnight.

For IF staining, the fixed samples were blocked with 5% goat (or donkey) serum in PBST (0.7% Triton X-100 in PBS) for 1 hour and incubated in primary antibodies (1:200 dilution) in blocking solution at 4°C overnight. After several washes, the samples were incubated in secondary antibodies (1:1000 dilution) in blocking solution at RT for 1 hour and nuclei were stained with 4′,6-diamidino-2-phenylindole (DAPI) (1:1000 dilution; Invitrogen). Then, they were

washed in PBST and mounted with Dako mounting medium (Agilent, S3023) for HUVECs and tumors and placed on microscope glass slides with VECTASHIELD (Vector Laboratories, H-1200) for retinas and aortic rings.

Primary antibodies used for IF staining were as follows: hamster anti-CD31 monoclonal (Millipore, MAB1398Z), rat anti-CD31 monoclonal (BD, 553370), rabbit anti-ERG monoclonal (Abcam, ab92513), goat anti-ESM1 polyclonal (R&D Systems, AF1999), goat anti-Dll4 polyclonal (R&D Systems, AF1389), rabbit anti-pERK1/2 monoclonal [Cell Signaling Technology (CST), #4370], rabbit anti-TAZ polyclonal (Sigma-Aldrich, HPA007415), rabbit anti-EEA1 monoclonal (CST, #3288), rabbit anti-pAkt1 (Ser^{473}) monoclonal (CST, #9018), rabbit anti-NF2 polyclonal (Thermo Fisher Scientific, HPA003097), mouse anti-NF2 monoclonal (Abcam, ab88957), mouse anti–VE-cadherin monoclonal (BD Biosciences, #555661), mouse anti-VEGFR2 monoclonal (Abcam, ab9530), rabbit anti-Rab5 monoclonal (CST, #3547), rabbit anti-Rab7 monoclonal (CST, #9367), rabbit anti-Rab11 monoclonal (CST, #3539), rabbit anti-Glut1 polyclonal (Millipore, 07-1401), rabbit anti-PlGF polyclonal (Bioss, BS-0280R), and sheep anti-ACKR1 polyclonal (Novus Biologicals, FAB6695P). Secondary antibodies were Cy3-, fluorescein isothiocyanate (FITC)–, or Cy5-conjugated anti-hamster IgG, anti-rat IgG, anti-rabbit IgG, anti-mouse IgG, anti-human IgG, anti-sheep IgG, or anti-goat IgG (Jackson ImmunoResearch). Reagents were as follows: biotin-conjugated isolectin B4 (IB4) (Sigma-Aldrich, L2140), Alexa Fluor 488– or Alexa Fluor 647–conjugated streptavidin (Invitrogen, S11223 and S21374), and Alexa Fluor 594–conjugated phalloidin (Thermo Fisher Scientific, A12381). For hematoxylin and eosin (H&E) staining of LLC tumors, they were fixed overnight in 4% PFA. After tissue processing using standard procedures, samples were embedded in paraffin and cut into 3-μm sections followed by H&E staining. To detect a hypoxic area in tumor, Hypoxyprobe-1 (60 mg/kg; solid pimonidazole hydrochloride, Natural Pharmacia International) was intraperitoneally injected 60 min before perfusion fixation. Then, the tumors were then harvested, sectioned, and stained with FITC-conjugated anti-Hypoxyprobe antibody. Images of all samples were obtained using a confocal microscope (Zeiss, LSM880) and processed with imaging software ZEN (Zeiss) and Adobe Photoshop (Adobe).

EdU incorporation assay for EC proliferation in the retinal vessels of neonatal mice
Six milligrams of EdU (Invitrogen, A10044) was dissolved in 1 ml of Milli-Q water as a stock solution. Then, 5 μl of the stock solution per gram of body weight was intraperitoneally injected 3 hours before the anesthesia. EdU-incorporated cells in the isolated retinas were detected with the Click-iT EdU Alexa Fluor 555 Imaging Kit (Invitrogen, C10338) according to the manufacturer's instructions.

Vascular leakage assay
For vascular leakage assay in the retina and thyroid glands, 50 μl of tetramethylrhodamine-conjugated dextran (25 mg/ml, 10 kDa; Sigma-Aldrich, D1816) and 50 μl of DyLight 488–conjugated *Lycopersicon esculentum* lectin (1.0 mg/ml; Vector Laboratories) were mixed and the mixture was intravenously injected into the mice. Ten minutes later, the retinas and thyroid glands were harvested and fixed in 4% PFA for 20 min. After washing with PBS, they were placed on microscope glass slides with VECTASHIELD.

Cell culture
Primary HUVECs were purchased from Lonza; cultured in EGM2 media (Lonza) at 37°C, 5% CO2, and 95% relative humidity; and used passages third to sixth for this study. HUVECs were plated at 1.25×10^4 per cm^2 for sparsely confluent culture and at 0.75×10^5 per cm^2 for densely confluent culture and incubated for 24 hours before the experiments.

RNA interference and migration assay in HUVECs
siRNA sequences were designed for human NF2 (5′-GAGGAAG-CAACCCAAGACG-3′) and GL2 (negative control; 5′-CGTACG-CGGAATACTTCGA-3′) according to the previous report (53). HUVECs were transfected with the siRNA using Lipofectamine RNAiMAX (Invitrogen) according to the manufacturer's protocol. The HUVECs were harvested 48 hours after transfection, and immunoblotting was performed to evaluate knockdown efficiency of Merlin. At 48 hours after siRNA transfection, the HUVECs were seeded on eight-well glass slide (Lab-Tek, 154534) and incubated until densely confluent. Then, scratch wounding was performed with a 10-μl pipette tip, and the cells were incubated with EGM-2 media for 9 hours.

Wound healing migration assay in cultured HUVECs
HUVECs were seeded at ~7 × 10^4 cells per each well of Culture-Insert 2 Well (Ibidi, #81176). After 24 hours of seeding, the insert was removed and filled with fresh EGM-2 medium. After 9 hours, images were taken and cell migration in the open wound area was quantified by ImageJ.

Ex vivo aortic ring assay
Aortic ring assay was performed as previously described (54). Aortas of the mice were harvested at the indicated days; incubated in Opti-MEM (Life Technologies) for 12 hours; cut into 1-mm-thick segments; embedded in type I collagen gel (Millipore) in a 96-well plate; incubated with Opti-MEM containing fetal bovine serum (FBS) (2%; HyClone) and VEGF (50 ng/ml; R&D Systems), Angpt2 (400 ng/ml; R&D Systems), bFGF (50 ng/ml; PeproTech), or LPA (5 μM; Sigma-Aldrich) for 2 days; and IF stained. Images for sprouting and microvessel growth were obtained using a Cell Observer (Carl Zeiss). Number of sprouts per ring was counted manually, and microvessel length from edge of aortic ring to the end of microvessel was measured using an ImageJ software [National Institutes of Health (NIH)].

RNA extraction and quantitative reverse transcription polymerase chain reaction
Total RNA was extracted from samples using RNeasy Mini Kit (QIAGEN) according the manufacturer's protocols. A total of 1 μg of extracted RNA was transcribed into cDNA using GoScript Reverse Transcription System (Promega). cDNA was mixed with primers and FastStart SYBR Green Master (Roche), and mRNA expression levels were measured by Real-Time PCR QuantStudio3 (Thermo Fisher Scientific). The primers were designed using Primer-BLAST and listed in table S1.

Filopodia formation assay in cultured HUVECs
HUVECs were seeded at ~7 × 10^4 cells per each well of into eight-well glass slide (Lab-Tek, 154534), transfected with siRNA, and incubated with 10% FBS containing EGM-2 medium for 48 hours. After scratching the wound with the 200-μl pipette tip, the cells were incubated with

10% FBS containing EGM-2 for 9 hours and then switched with serum-free EBM-2 and incubated for 12 hours. At 6 hours after VEGF (50 ng/ml) stimulation, filopodia formation was analyzed by IF staining.

In vivo VEGF internalization assay
After anesthesia of the neonates, we injected Alexa Fluor 488–labeled VEGF (0.5 μg in 0.5 μl) generated by Alexa Fluor 488 microscale protein labeling kit (A30006, Invitrogen) into vitreous cavity using Nanoliter 2000 micro-injector (World Precision Instruments) fitted with a glass capillary pipette and waited for indicated times. The retinas were harvested and IF stained as described above.

Immunoblotting and immunoprecipitation assays
For immunoblotting, the cells were lysed on ice in radioimmuno-precipitation assay lysis buffer supplemented with protease and phosphatase inhibitors (CST, #5872). Cell lysates were centrifuged for 10 min at 4°C and 12,000 rpm. Protein concentrations of the supernatants were quantitated using the detergent-insensitive Pierce BCA protein assay kit (Thermo Scientific, 23227). Sample loading buffer was added to total protein lysates, and samples were heated at 95°C for 5 min. Aliquots of each protein lysate (10 to 20 μg) were subjected to SDS–polyacrylamide gel electrophoresis. For immuno-precipitation analysis, cells were lysed on ice with NETN buffer [20 mM tris-HCl (pH 8.0), 100 mM NaCl, 1 mM EDTA, and 0.5% NP-40] with protease and phosphatase inhibitors (CST, #5872). Cell lysates were centrifuged, and the protein concentration of the supernatants were quantitated (Thermo Scientific, 23227) as above. Each supernatant of protein samples was incubated with anti-VEGFR2 antibody (CST, #2479) for 12 hours at 4°C. After 2-hour incubation of 35 μl of Pierce Protein A/G agarose (Thermo Scientific, 20421) at 4°C, agarose were washed in cold NETN buffer three times. In case of SBP-tagged retroviral infection, infected cell lysates were incubated with Pierce Streptavidin Agarose (Thermo Scientific, 20353) for 2 hours at 4°C without antibody incubation. Sample loading buffer was added, and the samples were denatured at 95°C for 5 min. Aliquots of each protein lysate (1 mg) were subjected to SDS–polyacrylamide gel electrophoresis. Normal rabbit IgG (CST, #2729) was used as a negative control. After electrophoresis, protein was transferred to nitrocellulose membranes and blocked for 30 min with 3% bovine serum albumin (BSA) in TBST (0.1% Tween 20 in tris-buffered saline). Primary antibodies were incubated overnight at 4°C. Primary antibodies used for immunoblotting were as follows: rabbit anti-p-VEGFR2 (Y1175) monoclonal (CST, #2478), rabbit anti–p-ERK1/2(Thr[202]/Tyr[204]) monoclonal (CST, #4370), mouse anti-NF2 monoclonal (Abcam, ab88957), rabbit anti–β-actin monoclonal (Sigma-Aldrich, A5441), rabbit anti-VEGFR2 monoclonal (CST, #2479), rabbit anti–VE-cadherin monoclonal (CST, #2500), rabbit anti-Tie2 monoclonal (CST, #7403), rabbit anti-VEGFR3 polyclonal (Abcam, ab27278), rabbit anti–p-NF2 (S518) polyclonal (Abcam, ab2478), mouse anti-Flag monoclonal (Sigma-Aldrich, F3165), and rabbit anti-GAPDH monoclonal (CST, #5174S). After washes, membranes were incubated with anti-rabbit (CST, #7074) or anti-mouse (CST, #7076) secondary peroxidase–coupled antibody for 1 hour at RT. Target proteins were detected using ECL Western blot detection solution (Millipore, WBKLS0500).

Retroviral generation and infection
SBP-Flag–tagged human *NF2* cDNA was cloned into the pMSCVpuro vector (Clontech, K1062-1) and designated "Flag-NF2 WT."

Nonphosphorylatable NF2 (Flag-NF2-S518A) and phosphomimetic NF2 (Flag-NF2-S518D) were generated by overlap extension poly-merase chain reaction (PCR) cloning. Partially overlapping mutant primers oriented in the inverse direction were used to amplify the point mutated-*NF2* cDNA and were cloned into pMSCV-puro vector. To generate retroviruses in human embryonic kidney 293T cells, the indicated vectors were transfected with the vectors encoding gag/pol (Addgene) and vesicular stomatitis virus glycoprotein (Addgene) using polyethylenimine hydrochloride (Polysciences, 24885-2) for 12 hours, and then, the culture medium was changed with a fresh medium. After 48 hours of transfection, medium was harvested and centrifuged to remove dead cells. HUVECs were in-fected with the retrovirus using polybrene (Sigma-Aldrich, TR-1003-G). The pMSCVpuro vector was used as a control vector.

In vitro VEGFR2 internalization assay
HUVECs were incubated for 12 hours in EBM-2 media, treated with VEGF (50 ng/ml), and incubated at 4°C for 30 min. Then, they were transferred to 37°C for indicated times. To stop the reaction and remove plasma membrane-bound VEGF, the cells were washed for 15 min with acid solution [PBS (pH 2.7), containing 25 mM glycine and 3% BSA]. The cells were washed with PBS, fixed, and IF stained with mouse anti-VEGFR2 monoclonal antibody (Abcam, Ab9530) and rabbit anti-Rab5 (CST, #3547) monoclonal, rabbit anti-Rab7 (CST, #9367) monoclonal, or rabbit anti-Rab11 (CST, #3539) monoclonal antibody for 12 hours and secondary antibody for 1 hour to detect internalized VEGFR2.

Subcutaneous LLC tumor model
LLC cells were obtained from American Type Culture Collection. To generate implanted LLC tumor models, suspensions of 1×10^6 LLC cells in 100 μl were subcutaneously injected into the dorsal flank of adult C57BL/6J mice at 1 week after or 6 days before the consecutive tamoxifen treatment. Tumor volumes were measured at indicated time points, and they were calculated according to the formula $0.5 \times A \times B^2$, where A is the longest diameter of a tumor and B is its perpendicular diameter. At indicated days later, the mice were anesthetized, and tumor tissues were harvested for further analyses.

In vivo perfusion assay
For a vascular perfusion analysis in the tumors, 100 μl of DyLight 488–conjugated *L. esculentum* lectin (1.0 mg/ml; Vector Laboratories) was intravenously injected via tail vein into the tumor bearing mice. At 30 min later, the mice were anesthetized and perfused with 1% PFA via intracardiac injection to remove circulating lectin, and tumors were harvested before being sacrificed. IF staining of tumor was performed as described above.

Morphometric analyses
Morphometric measurements of retinas, HUVECs, and tumors were performed by using the ImageJ software (NIH). Radial length of retinal vessel was measured as the distance from optic disc to the peripheral vascular front in the leaflet of retina and averaged. Number of branching points was measured manually in 200 μm–by–200 μm fields located between an artery and a vein at front in retina and averaged. Vascular density was measured as CD31^{+} retinal vessel area per total measured area of the retina and presented as %. A number of filopodia and sprouts were first measured in 200 μm–by–200 μm fields and then normalized to CD31^{+} vessel area in

200 μm–by–200 μm fields in the angiogenic front of retina. Dextran^{+} area subtracted from the lectin^{+} vessel area was regarded as extravascular dextran leakage area and presented as %. For thyroid gland and small intestine villi, the total number of filopodia was measured in 200 μm–by–200 μm fields and then normalized to a length of 100 μm along the blood capillaries. The total number of filopodia in HUVECs was measured in 50 μm–by–50 μm fields and then normalized to a length of 100 μm along the edge of the cells. The total number of filopodia in tdTomato reporter mouse was measured manually per tdTomato[+] cell. Density of blood vessels at peritumoral and intratumoral regions of tumor sections was measured in 500 μm–by–500 μm fields. Staining intensities were measured in regions of interest of vessels, tumor, and particular regions of HUVECs and averaged. ESM1^{+} ECs, pERK1/2^{+} ECs, Taz^{+} ECs, PlGF^{+} ECs, ACKR1^{+} ECs, vascular perfusion, and hypoxyprobe^{+} area were presented as percentages or fold changes per CD31^{+} area in 500 μm–by–500 μm fields. GLUT1^{+} hypoxic area was presented as percentages per total midsectional tumor area. Fluor-VEGF intensity was presented as percentage per CD31^{+} area in 20 μm–by–20 μm field. VEGF internalization intensity was presented as percentage per nucleus in 50 μm–by–50 μm field.

Isolation of mouse lung and brain ECs

After anesthesia, lungs were harvested at P6; cut into small pieces; and digested in buffer containing collagenase type II (Worthington), Dispase (Gibco, 17105041), and deoxyribonuclease (DNase) I (Roche, 10104159001) at 37°C for 30 min. Tissues were gently agitated, strained with a 100-μm nylon mesh to remove cell clumps, incubated in ACK lysis buffer for 2 min to remove erythrocytes, and strained with a 40-μm nylon mesh. Single-cell suspensions were incubated for 20 min with anti-CD45 Microbeads (Miltenyi). After depleting CD45^{+} cells using AutoMACS (Miltenyi), according to the manufacturer's instructions, anti-CD31 Microbeads (Miltenyi) were incubated for 20 min. After collecting CD31^{+} and CD31^{−} cells, cells were lysed for Western blot. For brain EC isolation, brains were harvested at P9; cut into small pieces; and digested in buffer containing papain (30 U/ml; Worthington), DNase (40 μg/ml; Worthington), and Liberase TM (0.125 mg/ml; Roche) at 37°C for 1 hour. After myelin removal by 20% albumin bovine (Biosesang), single-cell suspensions were incubated for 30 min with APC-conjugated rat anti-CD45 (559864, BD Biosciences). To discriminate dead cells, cells were stained with DAPI (Sigma-Aldrich) and CD45^{−} tdTomato^{+} cells were sorted with FACSAria II (BD Biosciences).

Bulk RNA sequencing and data analysis

RNA from the fluorescence-activated cell sorting (FACS)–sorted cells was isolated using the RNeasy Plus Micro Kit (QIAGEN) according to the manufacturer's instructions. RNA quality was checked using a 2100 Bioanalyzer (Agilent). RNA library construction was performed with the NEBNext Ultra II Directional RNA Library Prep Kit for Illumina (NEB) according to the manufacturer's instructions. Libraries were validated with the Bioanalyzer and Qubit Fluorometric Quantitation (Thermo Fisher Scientific). The NextSeq 500/550 mid Output v2 Kit was used for sequencing with a NextSeq 550 (Illumina) to generate 75–base pair pair-end reads. The quality assessment of raw sequence data was performed using FastQC (version: FastQC 0.11.3; www.bioinformatics.babraham.ac.uk/projects/fastqc/). No samples were discarded from the analysis. RNA-seq data analysis was performed as described previously (55) with some modifications.

Sequenced reads were aligned to the mm10 mouse genome assembly (GRCm38; the mouse genome was downloaded from the iGenomes portal) reference genome with STAR (version 2.7.3a), and the aligned reads were used to quantify mRNA expression by using HTSeq-count (version 0.6.1). Differentially expressed genes were presented using hypergeometric calculation implemented in the DESeq2 Bioconductor package in R statistical language. To identify genes with notable expression, we used scatter plotting and hierarchical clustering function in SeqMonk (version 1.45.4, Babraham Bioinformatics SeqMonk Project; www.bioinformatics.babraham.ac.uk/projects). Curated gene sets derived from the Kyoto Encyclopedia of Genes and Genomes pathway database and Broad Institute Molecular Signatures Database were used, and multiple lists of enriched gene sets were generated using the GSEA algorithm (56). GO analysis was performed with the g:Profiler (http://biit.cs.ut.ee/gprofiler/).

Droplet-based scRNA-seq

For scRNA-seq on LLC tumor ECs, FACS-sorted live ECs were collected from two mice for control group and three mice for Nf2[iΔEC] group. Live EC single cells were sorted to processed using 10X Chromium Single-Cell 3′Reagent Kit v3 (10X Genomics) according to the manufacturer's instructions. Briefly, sorted ECs were suspended in 2% BSA solution and mixed with RT reagent mix and RT primer then added to each channel of 10X chips. ECs were separated into Gel Beads in Emulsion where RNA transcripts from single cells were barcoded, and then, cDNA libraries were constructed and amplified. SPRI beads (Beckman Coulter) were used for appropriate size selection of cDNA, and products were ligated with adaptor and amplified by sample-index PCR. Double-sized size selections using SPRI beads were followed, and the final library constructs were diluted in 10-fold and ran on the Agilent Bioanalyzer High Sensitivity Chip for quality control. Single-cell library sequencing was conducted using Illumina HiSeq-X platform. The sequenced data of single-cell libraries were demultiplexed and aligned to mouse reference genome (mm10) by Cell Ranger software 3.0.0 provided by 10X Genomics. Raw expression matrices were then built by using Read10X function in Seurat (version 3.1.1). For cell-based quality control, low-quality cells detected with less than 500 and more than 8000 genes and putative dead cells with high mitochondrial gene percentage [>10% of total unique molecular identifier (UMI) counts] were discarded. For gene-based filtering, genes expressed in less than three cells were removed. After removal of unwanted cells and genes, normalization of raw expression matrices was performed by dividing UMI counts for each gene per cell by the total sum of UMI counts in a given cell, multiplied by 10,000 and log-transformed, producing log counts per million–like values. Then, gene-based scaling was performed while regressing out variables such as number of UMIs and mitochondrial gene percentage. For clustering and downstream analysis, R package Seurat was used. First, variable genes for datasets were identified by FindVariableFeatures function in Seurat with options: selection.method = "vst." Then, principal components analysis was performed, and top 20 principal components were used for further analysis including uniform manifold approximation and projection for two-dimensional visualization, building shared nearest neighborhood graph, and Louvain algorithm for cluster identification. After initial clustering, non-ECs (e.g., CD45^{+} hematopoietic origin and immune cells, PDGFR^{+} stromal cells and ECAM1^{+} epithelial cells, and others) were removed from the dataset. Last, another round of clustering was performed on remaining

PECAM1$^+$/VE-cadherin$^+$ cells. Cluster-specific marker genes were regarded as differentially expressed genes for each cluster identified using FindMarkers function in Seurat on the RNA assay of Seurat object with following options: test.use = "MAST," min.pct = 0.25, min.diff.pct = 0.25. For GO and pathway analyses, top 100 differentially expressed genes were used as input for Enrichr (*42*).

Transcriptional profile analysis of microarray data
GSEA was performed with v4.0.3 of the Molecular Signature Database (www.broadinstitute.org/gsea/msigdb), and the gene sets that were <0.05 nominal *P* value were stated.

Statistics and reproducibility
No statistical methods were used to predetermine sample size. The experiments were randomized and investigators were blinded to allocation during experiments and outcome analyses. All values are presented as means ± SD. Statistical significance was determined by the two-tailed unpaired *t* test between two groups or Welch's one-way analysis of variance (ANOVA) test followed by Dunnett's T3 for multiple group comparison. Statistical analysis was performed using GraphPad Prism 7.0 (GraphPad software) or the R statistical environment (http://r-project.org). Statistical significance was set to $P < 0.05$.

SUPPLEMENTARY MATERIALS
Supplementary material for this article is available at https://science.org/doi/10.1126/sciadv.abn2611

View/request a protocol for this paper from *Bio-protocol*.

REFERENCES AND NOTES
1. R. Blanco, H. Gerhardt, VEGF and Notch in tip and stalk cell selection. *Cold Spring Harb. Perspect. Med.* **3**, a006569 (2013).
2. I. Geudens, H. Gerhardt, Coordinating cell behaviour during blood vessel formation. *Development* **138**, 4569–4583 (2011).
3. C. Margadant, Positive and negative feedback mechanisms controlling tip/stalk cell identity during sprouting angiogenesis. *Angiogenesis* **23**, 75–77 (2020).
4. H. Gerhardt, M. Golding, M. Fruttiger, C. Ruhrberg, A. Lundkvist, A. Abramsson, C. Mitchell, K. Alitalo, D. Shima, C. Betsholtz, VEGF guides angiogenic sprouting utilizing endothelial tip cell filopodia. *J. Cell Biol.* **161**, 1163–1177 (2003).
5. H. Gerhardt, VEGF and endothelial guidance in angiogenic sprouting. *Organogenesis* **4**, 241–246 (2008).
6. M. E. Pitulescu, I. Schmidt, B. D. Giaimo, T. Antoine, F. Berkenfeld, F. Ferrante, H. Park, M. Ehling, D. Biljes, S. F. Rocha, U. H. Langen, M. Stehling, T. Nagasawa, N. Ferrara, T. Borggrefe, R. H. Adams, Dll4 and Notch signalling couples sprouting angiogenesis and artery formation. *Nat. Cell Biol.* **19**, 915–927 (2017).
7. M. Hellström, L.-K. Phng, J. J. Hofmann, E. Wallgard, L. Coultas, P. Lindblom, J. Alva, A.-K. Nilsson, L. Karlsson, N. Gaiano, K. Yoon, J. Rossant, M. L. Iruela-Arispe, M. Kalén, H. Gerhardt, C. Betsholtz, Dll4 signalling through Notch1 regulates formation of tip cells during angiogenesis. *Nature* **445**, 776–780 (2007).
8. M. Simons, E. Gordon, L. C.-Welsh, Mechanisms and regulation of endothelial VEGF receptor signalling. *Nat. Rev. Mol. Cell Biol.* **17**, 611–625 (2016).
9. A. K. Olsson, A. Dimberg, J. Kreuger, L. Claesson-Welsh, VEGF receptor signalling—In control of vascular function. *Nat. Rev. Mol. Cell Biol.* **7**, 359–371 (2006).
10. M. Nakayama, A. Nakayama, M. van Lessen, H. Yamamoto, S. Hoffmann, H. C. A. Drexler, N. Itoh, T. Hirose, G. Breier, D. Vestweber, J. A. Cooper, S. Ohno, K. Kaibuchi, R. H. Adams, Spatial regulation of VEGF receptor endocytosis in angiogenesis. *Nat. Cell Biol.* **15**, 249–260 (2013).
11. S. P. Herbert, D. Y. R. Stainier, Molecular control of endothelial cell behaviour during blood vessel morphogenesis. *Nat. Rev. Mol. Cell Biol.* **12**, 551–564 (2011).
12. M. Simons, An inside view: VEGF receptor trafficking and signaling. *Physiology (Bethesda)* **27**, 213–222 (2012).
13. J. Zink, M. Frye, T. Frömel, C. Carlantoni, D. John, D. Schreier, A. Weigert, H. Laban, G. Salinas, H. Stingl, L. Günther, R. Popp, J. Hu, B. Vanhollebeke, H. Schmidt, A. Acker-Palmer, T. Renné, I. Fleming, P. M. Benz, EVL regulates VEGF receptor-2 internalization and signaling in developmental angiogenesis. *EMBO Rep.* **22**, e48961 (2021).
14. M. Shibuya, L. C.-Welsh, Signal transduction by VEGF receptors in regulation of angiogenesis and lymphangiogenesis. *Exp. Cell Res.* **312**, 549–560 (2006).
15. J. Kim, Y. H. Kim, J. Kim, D. Y. Park, H. Bae, D. H. Lee, K. H. Kim, S. P. Hong, S. P. Jang, Y. Kubota, Y. G. Kwon, D. S. Lim, G. Y. Koh, YAP/TAZ regulates sprouting angiogenesis and vascular barrier maturation. *J. Clin. Invest.* **127**, 3441–3461 (2017).
16. F. Neto, A. K.-Bergmann, Y. T. Ong, S. Alt, A.-C. Vion, A. Szymborska, J. R. Carvalho, I. Hollfinger, E. B.-Klein, C. A. Franco, M. Potente, H. Gerhardt, YAP and TAZ regulate adherens junction dynamics and endothelial cell distribution during vascular development. *eLife* **7**, e31037 (2018).
17. X. Wang, A. F. Valls, G. Schermann, Y. Shen, I. M. Moya, L. Castro, S. Urban, G. M. Solecki, F. Winkler, L. Riedemann, R. K. Jain, M. Mazzone, T. Schmidt, T. Fischer, G. Halder, C. R. de Almodóvar, YAP/TAZ orchestrate VEGF signaling during developmental angiogenesis. *Dev. Cell* **42**, 462–478.e7 (2017).
18. Y. H. Kim, J. Choi, M. J. Yang, S. P. Hong, C. K. Lee, Y. Kubota, D. S. Lim, G. Y. Koh, A MST1-FOXO1 cascade establishes endothelial tip cell polarity and facilitates sprouting angiogenesis. *Nat. Commun.* **10**, 838 (2019).
19. A. M. Petrilli, C. Fernandez-Valle, Role of Merlin/NF2 inactivation in tumor biology. *Oncogene* **35**, 537–548 (2016).
20. S. W. Plouffe, Z. Meng, K. C. Lin, B. Lin, A. W. Hong, J. V. Chun, K. L. Guan, Characterization of hippo pathway components by gene inactivation. *Mol. Cell* **64**, 993–1008 (2016).
21. W. Li, J. Cooper, M. A. Karajannis, F. G. Giancotti, Merlin: A tumour suppressor with functions at the cell cortex and in the nucleus. *EMBO Rep.* **13**, 204–215 (2012).
22. A. I. McClatchey, M. Giovannini, Membrane organization and tumorigenesis—The NF2 tumor suppressor, Merlin. *Merlin. Genes Dev.* **19**, 2265–2277 (2005).
23. A. I. McClatchey, R. G. Fehon, Merlin and the ERM proteins—Regulators of receptor distribution and signaling at the cell cortex. *Trends Cell Biol.* **19**, 198–206 (2009).
24. T. Okada, M. Lopez-Lago, F. G. Giancotti, Merlin/NF-2 mediates contact inhibition of growth by suppressing recruitment of Rac to the plasma membrane. *J. Cell Biol.* **171**, 361–371 (2005).
25. M. Curto, A. I. McClatchey, Nf2/Merlin: A coordinator of receptor signalling and intercellular contact. *Br. J. Cancer* **98**, 256–262 (2008).
26. M. Curto, B. K. Cole, D. Lallemand, C. H. Liu, A. I. McClatchey, Contact-dependent inhibition of EGFR signaling by Nf2/Merlin. *J. Cell Biol.* **177**, 893–903 (2007).
27. P. A. Guerrero, W. Yin, L. Camacho, D. Marchetti, Oncogenic role of Merlin/NF2 in glioblastoma. *Oncogene* **34**, 2621–2630 (2015).
28. J. Cao, M. Ehling, S. März, J. Seebach, K. Tarbashevich, T. Sixta, M. E. Pitulescu, A. C. Werner, B. Flach, E. Montanez, E. Raz, R. H. Adams, H. Schnittler, Polarized actin and VE-cadherin dynamics regulate junctional remodelling and cell migration during sprouting angiogenesis. *Nat. Commun.* **8**, 2210 (2017).
29. K. H. Moon, H.-T. Kim, D. Lee, M. B. Rao, E. M. Levine, D.-S. Lim, J. W. Kim, Differential expression of NF2 in neuroepithelial compartments is necessary for mammalian eye development. *Dev. Cell* **44**, 13–28.e3 (2018).
30. K. Okabe, S. Kobayashi, T. Yamada, T. Kurihara, I. Tai-Nagara, T. Miyamoto, Y. S. Mukouyama, T. N. Sato, T. Suda, M. Ema, Y. Kubota, Neurons limit angiogenesis by titrating VEGF in retina. *Cell* **159**, 584–596 (2014).
31. S. F. Rocha, M. Schiller, D. Jing, H. Li, S. Butz, D. Vestweber, D. Biljes, H. C. A. Drexler, M. Nieminen-Kelhä, P. Vajkoczy, S. Adams, R. Benedito, R. H. Adams, Esm1 modulates endothelial tip cell behavior and vascular permeability by enhancing VEGF bioavailability. *Circ. Res.* **115**, 581–590 (2014).
32. M. Xin, Y. Kim, L. B. Sutherland, M. Murakami, X. Qi, J. McAnally, E. R. Porrello, A. I. Mahmoud, W. Tan, J. M. Shelton, J. A. Richardson, H. A. Sadek, R. Bassel-Duby, E. N. Olson, Hippo pathway effector Yap promotes cardiac regeneration. *Proc. Natl. Acad. Sci. U.S.A.* **110**, 13839–13844 (2013).
33. M. Xin, Y. Kim, L. B. Sutherland, X. Qi, J. M. Anally, R. J. Schwartz, J. A. Richardson, R. Bassel-Duby, E. N. Olson, Regulation of insulin-like growth factor signaling by Yap governs cardiomyocyte proliferation and embryonic heart size. *Sci. Signal.* **4**, ra70 (2011).
34. H. T. McMahon, E. Boucrot, Molecular mechanism and physiological functions of clathrin-mediated endocytosis. *Nat. Rev. Mol. Cell Biol.* **12**, 517–533 (2011).
35. L. von Kleist, W. Stahlschmidt, H. Bulut, K. Gromova, D. Puchkov, M. J. Robertson, K. A. MacGregor, N. Tomilin, A. Pechstein, N. Chau, M. Chircop, J. Sakoff, J. P. von Kries, W. Saenger, H. G. Kräusslich, O. Shupliakov, P. J. Robinson, A. McCluskey, V. Haucke, Role of the clathrin terminal domain in regulating coated pit dynamics revealed by small molecule inhibition. *Cell* **146**, 471–484 (2011).
36. H. Yamamoto, M. Ehling, K. Kato, K. Kanai, M. van Lessen, M. Frye, D. Zeuschner, M. Nakayama, D. Vestweber, R. H. Adams, Integrin β1 controls VE-cadherin localization and blood vessel stability. *Nat. Commun.* **6**, 6429 (2015).
37. J. Y. Jang, S. Y. Choi, I. Park, D. Y. Park, K. Choe, P. Kim, Y. K. Kim, B. J. Lee, M. Hirashima, Y. Kubota, J. W. Park, S. Y. Cheng, A. Nagy, Y. J. Park, K. Alitalo, M. Shong, G. Y. Koh, VEGFR2 but not VEGFR3 governs integrity and remodeling of thyroid angiofollicular unit in normal state and during goitrogenesis. *EMBO Mol. Med.* **9**, 750–769 (2017).

38. F. Zhang, G. Zarkada, J. Han, J. Li, A. Dubrac, R. Ola, G. Genet, K. Boyé, P. Michon, S. E. Künzel, J. P. Camporez, A. K. Singh, G. H. Fong, M. Simons, P. Tso, C. Fernández-Hernando, G. I. Shulman, W. C. Sessa, A. Eichmann, Lacteal junction zippering protects against diet-induced obesity. *Science* **361**, 599–603 (2018).

39. J. S. Park, I. K. Kim, S. Han, I. Park, C. Kim, J. Bae, S. J. Oh, S. Lee, J. H. Kim, D. C. Woo, Y. He, H. G. Augustin, I. Kim, D. Lee, G. Y. Koh, Normalization of tumor vessels by Tie2 activation and Ang2 inhibition enhances drug delivery and produces a favorable tumor microenvironment. *Cancer Cell* **30**, 953–967 (2016).

40. Q. Zhao, A. Eichten, A. Parveen, C. Adler, Y. Huang, W. Wang, Y. Ding, A. Adler, T. Nevins, M. Ni, Y. Wei, G. Thurston, Single-cell transcriptome analyses reveal endothelial cell heterogeneity in tumors and changes following antiangiogenic treatment. *Cancer Res.* **78**, 2370–2382 (2018).

41. S. H. Jeong, M. J. Yang, S. Choi, J. M. Kim, G. Y. Koh, Refractoriness of STING therapy is relieved by AKT inhibitor through effective vascular disruption in tumour. *Nat. Commun.* **12**, 4405 (2021).

42. M. V. Kuleshov, M. R. Jones, A. D. Rouillard, N. F. Fernandez, Q. Duan, Z. Wang, S. Koplev, S. L. Jenkins, K. M. Jagodnik, A. Lachmann, M. G. McDermott, C. D. Monteiro, G. W. Gundersen, A. Ma'ayan, Enrichr: A comprehensive gene set enrichment analysis web server 2016 update. *Nucleic Acids Res.* **44**, W90–W97 (2016).

43. E. I. Surace, C. A. Haipek, D. H. Gutmann, Effect of merlin phosphorylation on neurofibromatosis 2 (NF2) gene function. *Oncogene* **23**, 580–587 (2004).

44. M. G. Lampugnani, A. Zanetti, M. Corada, T. Takahashi, G. Balconi, F. Breviario, F. Orsenigo, A. Cattelino, R. Kemler, T. O. Daniel, E. Dejana, Contact inhibition of VEGF-induced proliferation requires vascular endothelial cadherin, beta-catenin, and the phosphatase DEP-1/CD148. *J. Cell Biol.* **161**, 793–804 (2003).

45. D. Hanahan, R. A. Weinberg, Hallmarks of cancer: The next generation. *Cell* **144**, 646–674 (2011).

46. O. Casanovas, D. J. Hicklin, G. Bergers, D. Hanahan, Drug resistance by evasion of antiangiogenic targeting of VEGF signaling in late-stage pancreatic islet tumors. *Cancer Cell* **8**, 299–309 (2005).

47. J. M. L. Ebos, R. S. Kerbel, Antiangiogenic therapy: Impact on invasion, disease progression, and metastasis. *Nat. Rev. Clin. Oncol.* **8**, 210–221 (2011).

48. H. K. Wong, A. Shimizu, N. D. Kirkpatrick, I. Garkavtsev, A. W. Chan, E. di Tomaso, M. Klagsbrun, R. K. Jain, Merlin/NF2 regulates angiogenesis in schwannomas through a Rac1/semaphorin 3F-dependent mechanism. *Neoplasia* **14**, 84–94 (2012).

49. L. M. Ellis, D. J. Hicklin, VEGF-targeted therapy: Mechanisms of anti-tumour activity. *Nat. Rev. Cancer* **8**, 579–591 (2008).

50. Z. Zhang, K. G. Neiva, M. W. Lingen, L. M. Ellis, J. E. Nör, VEGF-dependent tumor angiogenesis requires inverse and reciprocal regulation of VEGFR1 and VEGFR2. *Cell Death Differ.* **17**, 499–512 (2010).

51. I. Noguera-Troise, C. Daly, N. J. Papadopoulos, S. Coetzee, P. Boland, N. W. Gale, H. Chieh Lin, G. D. Yancopoulos, G. Thurston, Blockade of Dll4 inhibits tumour growth by promoting non-productive angiogenesis. *Nature* **444**, 1032–1037 (2006).

52. G. Thurston, I. Noguera-Troise, G. D. Yancopoulos, The Delta paradox: DLL4 blockade leads to more tumour vessels but less tumour growth. *Nat. Rev. Cancer* **7**, 327–331 (2007).

53. M. Kim, M. Kim, S. J. Park, C. Lee, D. S. Lim, Role of angiomotin-like 2 mono-ubiquitination on YAP inhibition. *EMBO Rep.* **17**, 64–78 (2016).

54. M. Baker, S. D. Robinson, T. Lechertier, P. R. Barber, B. Tavora, G. D'Amico, D. T. Jones, B. Vojnovic, K. Hodivala-Dilke, Use of the mouse aortic ring assay to study angiogenesis. *Nat. Protoc.* **7**, 89–104 (2011).

55. H. W. Jeong, B. H.-Rodríguez, J. M. Kim, K. P. Kim, R. Enriquez-Gasca, J. Yoon, S. Adams, H. R. Schöler, J. M. Vaquerizas, R. H. Adams, Transcriptional regulation of endothelial cell behavior during sprouting angiogenesis. *Nat. Commun.* **8**, 726 (2017).

56. A. Subramanian, P. Tamayo, V. K. Mootha, S. Mukherjee, B. L. Ebert, M. A. Gillette, A. Paulovich, S. L. Pomeroy, T. R. Golub, E. S. Lander, J. P. Mesirov, Gene set enrichment analysis: A knowledge-based approach for interpreting genome-wide expression profiles. *Proc. Natl. Acad. Sci. U.S.A.* **102**, 15545–15550 (2005).